VLA Survey of Dense Gas in Extended Green Objects: Prevalence of 25 GHz Methanol Masers

A. P. M. Towner[1,2,7], C. L. Brogan[1], T. R. Hunter[1], C. J. Cyganowski[3], B. A. McGuire[1,6], R. Indebetouw[1,2], R. K. Friesen[4], and C. J. Chandler[5]

[1] National Radio Astronomy Observatory, 520 Edgemont Rd., Charlottesville, VA 22903, USA
[2] Department of Astronomy, University of Virginia, P.O. Box 3818, Charlottesville, VA 22903, USA
[3] Scottish Universities Physics Alliance (SUPA), School of Physics and Astronomy, University of St. Andrews, North Haugh, St Andrews, Fife KY16 9SS, UK
[4] Dunlap Institute for Astronomy and Astrophysics, University of Toronto, 50 St George St., Toronto, ON, M5S 3H4, Canada
[5] National Radio Astronomy Observatory, 1003 Lopezville Rd., Socorro, NM 87801, USA

Abstract

We present $\sim 1''$–$4''$ resolution Very Large Array (VLA) observations of four CH_3OH J_2–J_1-E 25 GHz transitions ($J = 3, 5, 8, 10$) along with the 1.3 cm continuum toward 20 regions of active massive star formation containing Extended Green Objects (EGOs), 14 of which we have previously studied with the VLA in the Class I 44 GHz and Class II 6.7 GHz maser lines. Sixteen regions are detected in at least one 25 GHz line ($J = 5$), with 13 of 16 exhibiting maser emission. In total, we report 34 new sites of CH_3OH maser emission and 10 new sites of thermal CH_3OH emission, significantly increasing the number of 25 GHz Class I CH_3OH masers observed at high angular resolution. We identify probable or likely maser counterparts at 44 GHz for all 15 of the 25 GHz masers for which we have complementary data, providing further evidence that these masers trace similar physical conditions despite uncorrelated flux densities. The sites of thermal and maser emission of CH_3OH are both predominantly associated with the 4.5 μm emission from the EGO, and the presence of thermal CH_3OH emission is accompanied by 1.3 cm continuum emission in 9 out of 10 cases. Of the 19 regions that exhibit 1.3 cm continuum emission, it is associated with the EGO in 16 cases (out of a total of 20 sites), 13 of which are new detections at 1.3 cm. Twelve of the 1.3 cm continuum sources are associated with 6.7 GHz maser emission and likely trace deeply embedded massive protostars.

Key words: ISM: jets and outflows – masers – stars: formation – stars: massive – techniques: interferometric

1. Introduction

Massive young stellar objects (MYSOs) remain embedded in their parent clouds during the early stages of their evolution, making them difficult to observe directly. MYSOs also evolve more quickly than lower-mass young stellar objects (YSOs), making MYSOs rare and especially difficult to observe during their early stages of evolution. Furthermore, MYSOs frequently form in clustered environments, leading to a confusion problem, and tend to be at large distances ($>$1 kpc), leading to resolution limitations. One particularly crucial stage of MYSO evolution is the phase in which the object is actively accreting matter and driving outflows. While the process of mass accretion for low-mass stars is fairly well understood (Yorke et al. 1993), it is thought that MYSOs continue to accrete even after hydrogen burning has commenced in the core (Stahler et al. 2000), and it is this continued mass transfer onto the protostar that leads to the formation of massive stars (Zinnecker & Yorke 2007). However, this process of mass transfer, being as it is both heavily obscured and comparatively short-lived, is not observationally well-constrained.

Recent observations have aimed to investigate the observational markers of MYSOs in this critical phase of their evolution. Cyganowski et al. (2008) identified $>$300 sources with extended 4.5 μm emission in the GLIMPSE-I survey images (Benjamin et al. 2003; Churchwell et al. 2009); these extended 4.5 μm sources are strongly correlated with infrared dark clouds (IRDCs) and 6.7 GHz Class II CH_3OH masers. The 4.5 μm sources were classified as Extended Green Objects (EGOs) by Cyganowski

et al. (2008), for the common coding of the 4.5 μm band as green in three-color composite *Spitzer* InfraRed Array Camera (IRAC) images. EGOs lie in a region of mid-infrared (MIR) color–color space consistent with protostars that are still in infalling envelopes; the extended "green" emission is thought to arise from shocked H_2 emission in the 4.5 μm band. Furthermore, because IRDCs mark the earliest stages of high-mass star formation (Rathborne et al. 2006, 2007), and 6.7 GHz Class II CH_3OH masers are radiatively pumped and associated exclusively with massive YSOs (Cragg et al. 1992; Szymczak et al. 2005; Ellingsen 2006), Cyganowski et al. (2008) concluded that EGOs must trace massive protostars that are actively accreting and driving outflows. From the $>$300 identified EGO sources, a sample of $\sim$20 objects was selected for follow-up observations in the Class I 44 GHz and Class II 6.7 GHz CH_3OH maser lines and in the outflow tracers HCO^+ and SiO (Cyganowski et al. 2009). Class I 44 GHz CH_3OH masers were detected toward 90% of the sample. Both the HCO^+ line profiles and SiO detections indicated the presence of active outflows in much of the sample, supporting the idea that Class I masers, which are primarily collisionally pumped, trace the impact of outflows on dense gas in star-forming regions (e.g., Plambeck & Menten 1990; Johnston et al. 1992; Kurtz et al. 2004; Voronkov et al. 2006).

Originally discovered in Orion-KL (Barrett et al. 1971, 1975), the Class I CH_3OH J_2–J_1-E transitions at 25 GHz form a ladder with energy levels from $\sim$20–140 K for $J = 2$–10 (for a rotational level diagram, see Leurini et al. 2016). Higher resolution observations soon confirmed the suspicion that the emission in these lines arises from maser action (Hills et al. 1975). The first interferometric studies ($J = 6$ and 7) noted a correspondence in the maser positions with 2 μm H_2

---

emission, thus associating them with shocked gas (Matsakis et al. 1980). Further studies of these transitions in other objects find that their intensity usually peaks around $J = 6$, and that they are not always inverted but do consistently trace regions of high density and temperature (Menten et al. 1986, 1988). Statistical equilibrium calculations using the large velocity gradient approach confirm that in gas at $\sim$200 K, the $J = 6$ maser can occur at densities of $5 \times 10^{(5-8)}$ cm^{-3} (Leurini et al. 2016). The 25 GHz transitions are thought to probe a similar, but narrower, range of physical conditions compared to the other two families of Class I CH$_3$OH masers (44/95 and 36/84 GHz, Sobolev et al. 2007). Thus, interferometric observations of the 25 GHz lines combined with interferometric observations of other Class I transitions (e.g., Voronkov et al. 2007, 2012) are important to further refine the physical conditions that the 25 GHz lines typically trace.

In this paper, we present a 1.3 cm Karl G. Jansky Very Large Array (VLA) survey of 20 GLIMPSE EGOs in continuum and several CH$_3$OH transitions. The majority of our targets are selected from the GLIMPSE-I EGO catalog of Cyganowski et al. (2008); only one, G08.67−0.35, is in the GLIMPSE-II survey area (this source is G08.67−0.36 in the GLIMPSE-II EGO catalog of Chen et al. 2013). Table 1 summarizes salient information about our target EGOs. We describe the observations in Section 2, present our results in Section 3, discuss the results in Section 4, and summarize our conclusions in Section 5.

2. 1.3 cm (25 GHz) VLA Observations

We used the VLA (Perley et al. 2011) to observe 20 EGOs at 1.3 cm (25 GHz). Table 2 summarizes the project AB1346 phase centers, observing dates, configuration(s), and phase calibrator for each target EGO. The observations were taken under the Resident Shared Risk Observing (RSRO) program (Chandler & Butler 2014) using 16×8 MHz spectral windows (each with 256 channels and single polarization) to observe four transitions of CH$_3$OH, as well as the NH$_3$ (1,1) through (6,6) metastable transitions and the H63α and H64α radio recombination lines (RRLs). The four remaining spectral windows were placed to cover additional possible, but unlikely to be detected, species of interest. The primary purpose of these "extra" spectral windows is for continuum, and indeed, none of these transitions were detected. In this paper, we focus on the 1.3 cm continuum and CH$_3$OH data; the details of the observed CH$_3$OH transitions are given in Table 3. Hereafter, the CH$_3$OH transitions will be denoted by the first two values of their upper state quantum number, for example $J'(K_a, K_c)–J''(K_a, K_c) = 3$ (2, 1)–3(1, 2) will be 3_2, etc.

The data were calibrated and imaged using the CASA software package. For all sources, the bandpass calibrator was J1924−2914. For all but two sources, 3C 286 (J1331+3030), combined with a model for its flux distribution, was used for absolute flux calibration. The two exceptions (where the 3C 286 observations failed to provide viable data) were G16.59−0.05 and G35.03+0.35. For these two sources, the derived flux density for the nearest other observation of the same phase calibrator (in time) was used to set the absolute flux scale. Opacities as a function of frequency were derived from the VLA seasonal model.[8] We expect the absolute flux calibration

---

[8] See EVLA Memo 143, VLA Test Memo 232, and VLA Scientific Memo 176. All three memos are archived at http://library.nrao.edu/vla.shtml.

to be good to $\sim$10%. Where necessary, antenna position corrections were also applied.

After the standard calibration was applied, "line" data sets were created by removing the continuum in the uv-plane using line-free channels in each spectral window. A few of the EGOs have bright, compact continuum sources in the VLA field of view (FOV) that are not at the phase center: G08.67−0.35, G11.92−0.61, and G28.28−0.36. In these cases, it was necessary to first shift the phase center to the brightest continuum source in the FOV, and then shift back after continuum subtraction to avoid aliasing effects. After continuum subtraction, the 31.25 kHz channel width ($\sim$0.38 km s^{-1}) line data were Hanning smoothed and imaged with a velocity channel width of 0.4 km s^{-1}. The D-configuration sources were imaged with a robust parameter of 0.75, while the CnB and C configuration data (see Table 2) were imaged with robust = 1.0.

The continuum for each EGO comprises 30 MHz of bandwidth from the four "extra" transition spectral windows, plus an additional 15 MHz from the line-free regions of the spectral windows covering the four CH$_3$OH transitions. Fields without RRL detections in the FOV have an additional 7.5 MHz of continuum bandwidth. The continuum images were made with multifrequency synthesis and robust = 1.0 for targets with only weak continuum emission in the FOV, and more uniform weighting and/or a restricted short spacing uv range when diffuse/confusing sources are present. The median geometric means of the synthesized beam in the D, C, and CnB configurations are 3″.32, 1″.03, and 0″.69, respectively (the source with D and CnB configuration data is included in the CnB median). The imaged fields of view for both the line and continuum images are similar to the 2′ full width to half power of the 25 m VLA dishes at 1.3 cm; primary beam correction was applied to all images.

3. Results

Figures 1 and 2 show three-color mid-infrared *Spitzer* GLIMPSE (Benjamin et al. 2003; Churchwell et al. 2009) images of our EGO targets. In both figures, contours of the new VLA 1.3 cm continuum data are overlaid in red. We also overlay 24 μm contours from the MIPS/*Spitzer* Survey of the Galactic Plane (MIPSGAL; Carey et al. 2009) in yellow. Figure 1 shows the 16 targets for which we detected 25 GHz CH$_3$OH emission. Figure 2 shows the two targets for which we detected 1.3 cm continuum emission in the vicinity of the EGO but no 25 GHz CH$_3$OH emission. Note that the two sources (G18.89−0.47 and G25.27−0.43) for which neither 1.3 cm continuum nor 25 GHz CH$_3$OH emission was detected in the vicinity of the EGO are not shown.

3.1. 1.3 cm Continuum Emission

We detect 1.3 cm continuum emission within the 2′ FOV for 19 of the 20 observed fields (only G18.89−0.47 lacks any detectable emission). However, detectable 1.3 cm emission in the vicinities of the EGOs themselves (i.e., within or touching the boundary of the extended 4.5 μm emission) is only detected toward 16 of the 20 fields for a detection rate of 80% (Figures 1 and 2). A few of these have more than one distinct region of emission, bringing the total number of individual EGO-associated 1.3 cm detections to 20. The positions and properties of the EGO-associated 1.3 cm continuum detections are detailed in Table 4.

Table 1
EGO Source Properties

Source	V_{LSR}[a] (km s^{-1})	Distance[b] (kpc)	EGO[c] Cat	IRDC[d]	H2O[e] Maser	CH$_3$OH Masers (GHz)[f] 6.7[g]	44[h]	95[i]
G08.67−0.35	35	4.1	C13	N	Y	Y	Y	Y
G10.29−0.13	14	1.9	2	Y	Y	Y	Y	Y
G10.34−0.14	12	1.6	2	Y	Y	Y	Y	Y
G11.92−0.61	36	$3.38^{+0.33}_{-0.27}$ (3.5)	1	Y	Y	Y	Y	Y
G12.68−0.18	55	$2.40^{+0.17}_{-0.15}$ (4.4)	4	Y	Y	Y	?	Y
G12.91−0.03	57	4.5	1	Y	Y	Y	?	Y
G14.33−0.64	23	$1.13^{+0.14}_{-0.11}$ (2.3)	1	Y	Y	?	Y	Y
G14.63−0.58	19	$1.83^{+0.08}_{-0.07}$ (1.9)	1	Y	Y	Y	?	Y
G16.59−0.05	60	$3.58^{+0.32}_{-0.27}$ (4.2)	2	N	Y	Y	?	Y
G18.67+0.03	80	4.8	1	N	Y	Y	Y	Y
G18.89−0.47	66	4.2	1	Y	Y	Y	Y	Y
G19.36−0.03	27	2.2	2	Y	N	Y	Y	Y
G22.04+0.22	51	3.4	1	Y	Y	Y	Y	Y
G24.94+0.07	42	2.8	1	N	Y	Y	Y	Y
G25.27−0.43	60	3.6	1	Y	Y	Y	Y	Y
G28.28−0.36	49	3.0	2	Y	N	Y	N	N
G28.83−0.25	87	4.8	1	Y	Y	Y	Y	?
G35.03+0.35	53	$2.32^{+0.24}_{-0.20}$ (3.2)	1	Y	Y	Y	Y	Y
G45.47+0.05	61	$8.40^{+1.4}_{-1.1}$ (7.1)	1	Y	Y	N	N	N
G49.27−0.34	68	5.4	1	Y	Y	N	Y	Y

Notes.

[a] LSRK velocities are the single-dish NH$_3$ (1,1) values from Cyganowski et al. (2013), except for G08.67−0.35, which is the CH$_3$CN value from Purcell et al. (2006).

[b] Distances without errors are estimated from the LSRK velocity and the Galactic rotation curve parameters from Reid et al. (2014). Parallax distances (with their uncertainties) are given where available from Reid et al. (2014 and references therein), with the kinematic distance in parentheses for comparison. All kinematic distances are the near distance, except for G45.47+0.05 and G49.27−0.34 (which are in the direction of tangent points); for the former source we use the parallax distance for G45.45+0.05, which is an H II region 1′ west of the EGO.

[c] Except for G08.67−0.35, this is the table number of the EGO in Cyganowski et al. (2008). In that paper, Tables 1 and 2 list "likely" EGOs for which the five-band (3.6–24 μm) or only 4.5 μm *Spitzer* photometry can be measured, respectively. Table 4 lists "possible" EGO outflow candidates for which only 4.5 μm photometry is possible. G08.67−0.35 is from Chen et al. (2013).

[d] Coincidence of EGO with IRDC as indicated by Cyganowski et al. (2008), except for G08.67−0.35 (Chen et al. 2013).

[e] Water maser data from the Cyganowski et al. (2013) Nobeyama 45 m survey of EGOs, except for G08.67−0.35, which comes from Hofner & Churchwell (1996) (VLA) and Breen & Ellingsen (2011; ATCA).

[f] Sources for which we could find no information in the literature are indicated by a "?"

[g] The 6.7 GHz maser detection information comes from Cyganowski et al. (2009) using the VLA, except for G08.67−0.35, G12.68−0.18, G12.91−0.03, G14.63−0.58, G16.59−0.05, and G45.47+0.05, which come from Green et al. (2010 and references therein) and used the ATCA.

[h] Information for 44 GHz masers come from the VLA and were taken from Cyganowski et al. (2009), except for G08.67−0.35 (Gómez et al. 2010) and G45.47+0.05 (Kang et al. 2015).

[i] Most information for 95 GHz masers were taken from Chen et al. (2011) using the Mopra 22 m telescope. The exceptions are G08.67−0.35 and G14.33−0.64 from Val'tts et al. (2000) using Mopra, G35.03+0.35 from Kang et al. (2015) using the Korean VLBA Network, and G16.59−0.05 and G49.27−0.34 from Chen et al. (2012) using the Purple Mountain Observatory 13.7 m telescope.

Despite the modest aggregate continuum bandwidth obtainable from the relatively narrow spectral windows (see Section 2), in many cases these data represent the most sensitive centimeter-wavelength (cm-λ) observations of these sources to date. For example, 12 EGOs in our sample were also included in the 1.3 and 3.6 cm VLA EGO continuum survey of Cyganowski et al. (2011b, resolution ∼1″). With the exception of G10.29−0.13 (which is severely dynamic-range limited by emission from a bright H II region in the field), our new 1.3 cm images are a factor of 2–4 more sensitive than those of Cyganowski et al. (2011a).

Of our 20 EGO-associated continuum detections, 13 are new detections at 1.3 cm and have a median peak intensity of 0.50 mJy beam^{-1}. Of these, seven are new detections at any cm-λ. Columns 6–9 of Table 4 list previous detections of each source at 1.3 cm and other cm-λ. References for previously detected sources, as well as alternate names where applicable, are listed in columns 7 and 9 and associated table notes. It is notable that if it had been previously observed at 1.3 cm, it is very likely that G08.67−0.35_CM1 would have been detected at past sensitivity levels. The other 12 new 1.3 cm detections, with a median peak intensity of 0.42 mJy beam^{-1}, are sufficiently weak that these are the first (published) data with the sensitivity to detect them. Sub-mJy emission at 1.3 cm (at kiloparsec distances) can be due to either free–free emission from protostellar winds/jets or hypercompact H II regions, or alternatively the Rayleigh–Jeans tail of dust emission (see, for example, Brogan et al. 2016). In Section 3.3, we discuss the morphology of the 1.3 cm continuum emission and its relationship to the target EGO for individual sources, and compare with other cm-λ data where possible. Unfortunately, the absence (for the most part) of data at a second cm-λ with resolution and sensitivity comparable to our 1.3 cm images precludes systematic analysis of the underlying emission mechanism(s).

Table 2
Observing Parameters

Source	Pointing Center (J2000)		Config.	Date	Phase Cal.	Synth. Beam[a]	Line rms[b]	Cont. rms
	R.A.	Decl.				$'' \times ''$ [P.A.(°)]	(mJy beam^{-1})	(mJy beam^{-1})
G08.67−0.35	18 06 18.3	−21 37 31	CnB	2011 Jan 22 and Feb 05	J1820-2528	0.81 × 0.59 [65.4]	1.26	0.12
G10.29−0.13	18 08 49.3	−20 05 57	D	2010 Sep 13	J1820-2528	4.52 × 2.38 [14.0]	5.82	0.31
G10.34−0.14	18 09 00.0	−20 03 35	D	2010 Sep 09	J1820-2528	5.15 × 2.51 [21.4]	6.50	0.29
G11.92−0.61	18 13 58.1	−18 54 17	D and CnB	2010 Aug 25 and 2011 Jan 30	J1820-2528	1.30 × 0.87 [−7.3]	2.88	0.08
G12.68−0.18	18 13 54.7	−18 01 47	CnB	2011 Jan 29	J1832-2039	0.87 × 0.54 [71.0]	1.54	0.06
G12.91−0.03	18 13 48.2	−17 45 39	C	2010 Dec 11	J1832-2039	1.47 × 0.86 [−176.0]	2.80	0.05
G14.33−0.64	18 18 54.4	−16 47 46	D	2010 Sep 10	J1832-2039	4.63 × 2.45 [20.0]	5.20	0.10
G14.63−0.58	18 19 15.4	−16 30 07	D	2010 Sep 12	J1832-2039	4.42 × 2.50 [11.4]	3.73	0.06
G16.59−0.05	18 21 09.1	−14 31 48	C	2011 Jan 17	J1832-1035	1.37 × 0.89 [−0.9]	3.54	0.07
G18.67+0.03	18 24 53.7	−12 39 20	C	2011 Jan 07	J1832-1035	1.31 × 0.81 [−2.4]	2.03	0.04
G18.89−0.47	18 27 07.9	−12 41 36	C	2010 Dec 31	J1832-1035	1.36 × 0.82 [−4.0]	2.89	0.06
G19.36−0.03	18 26 25.8	−12 03 57	D	2010 Aug 22	J1832-1035	4.62 × 2.67 [22.6]	6.43	0.11
G22.04+0.22	18 30 34.7	−09 34 47	D	2010 Aug 30	J1832-1035	4.02 × 2.64 [19.0]	6.60	0.11
G24.94+0.07	18 36 31.5	−07 04 16	D	2010 Sep 03	J1832-1035	4.05 × 2.78 [26.7]	3.90	0.09
G25.27−0.43	18 38 56.9	−07 00 48	C	2011 Jan 06	J1832-1035	1.27 × 1.05 [19.5]	3.73	0.05
G28.28−0.36	18 44 13.2	−04 18 04	D	2010 Sep 05	J1832-1035	3.18 × 2.33 [−4.8]	5.31	0.17
G28.83−0.25	18 44 51.3	−03 45 48	C	2011 Jan 08	J1851+0035	1.16 × 0.83 [−8.8]	2.29	0.05
G35.03+0.35	18 54 00.5	+02 01 18	D	2010 Sep 07	J1851+0035	3.75 × 2.81 [−51.9]	4.51	0.10
G45.47+0.05	19 14 25.6	+11 09 28	C	2010 Dec 12 and 24	J1922+1530	0.99 × 0.82 [−19.7]	1.62	0.09
G49.27−0.34	19 23 06.7	+14 20 13	C	2010 Dec 19	J1922+1530	0.95 × 0.83 [−34.4]	2.90	0.07

Notes.
[a] Synthesized beam of the CH_3OH-E 5(2,3)–5(1,4) transition.
[b] Median rms noise per channel in the CH_3OH-E 5(2,3)–5(1,4) image cubes. The rms noise in a channel with bright maser emission will be significantly higher due to dynamic range limitations.

Table 3
Observed CH_3OH Transitions[a]

Species	Resolved QNs	Frequency[b] (GHz)	E_{upper} (K)	$S_{ij}\mu^2$ (D^2)
CH_3OH-E	3(2,1)–3(1,2)	24.928707(7)	36.17	2.8073
CH_3OH-E	5(2,3)–5(1,4)	24.9590789(4)	57.07	5.0264
CH_3OH-E	8(2,6)–8(1,7)	25.2944165(2)	105.84	8.3910
CH_3OH-E	10(2,8)–10(1,9)	25.8782661(4)	149.97	10.7398

Notes.
[a] Transition properties taken from Müller et al. (2004).
[b] Numbers in parentheses denote the measurement uncertainties in units of the least significant figure.

3.2. 25 GHz CH_3OH Emission

Of the four observed CH_3OH transitions, the 5_2 transition (see Table 3) is by far the most prevalent. Indeed, we detected this transition toward 16 of the 20 EGOs in the sample. In order to quantify the properties of the CH_3OH emission, which is mostly very compact, we used the imfit task in CASA to fit two-dimensional Gaussians to each distinct emission component channel by channel. We limited the fitting to regions with emission $>4\sigma$, where σ was measured locally to accurately assess the variable rms noise due to dynamic range limitations. The resulting fitted parameters for the position, velocity of peak emission, velocity range of emission, size, and flux density are given in Table 5. The position, peak velocity, fitted flux density, and fitted size for each distinct spatial component are taken from the channel with the highest flux density for the 5_2 transition; only the fitted flux density in the peak channel is given for the other three transitions. The distinct emission regions are named by their galactic EGO name followed by a letter of the alphabet in order of increasing R.A.

3.2.1. Distinguishing Maser and Thermal Emission

After fitting, we examined the properties of each distinct emission component and classified it as either maser or thermal emission. Ideally, we would use the line brightness temperature T_B to discriminate between maser and thermal emission (i.e., T_B exceeding a realistic thermal molecular gas temperature must be maser emission). For example, there are seven CH_3OH components with 5_2 T_B in excess of 1000 K, with a maximum of 10^5 K for G08.67−0.35_h (see Table 5) that are clearly due to non-thermal emission. However, due to the relatively poor angular resolution of some of the data, especially those observed only in the D-configuration (see Table 2), the current T_B lower limits are not always constraining. This is particularly problematic because EGOs are thought to harbor massive star formation, and relatively warm thermal gas (few 100 K) is a natural consequence. Indeed, some of the observed EGOs are known to harbor hot core line emission with gas temperatures as high as a few 100 K (see, e.g., Brogan et al. 2011; Cyganowski et al. 2011b, 2014, 2012; Ilee et al. 2016). In a few cases, the 25 GHz CH_3OH emission observed with the VLA is clearly thermal in origin, as evidenced by spectral breadth (several km s^{-1}) and/or large fitted emission size (i.e., significantly larger than the beam).

To distinguish the emission mechanism for modest T_B cases, we used two separate methods of analysis. The first uses the integer channel width (number of consecutive channels with emission $\geqslant 4\sigma$ at the location of interest) and fitted angular size

as discriminators. Spectrally broad ($\geqslant 4\sigma$ in $\geqslant 5$ channels, 2.0 km s^{-1}) emission with a large spatial extent (i.e., significantly spatially resolved fits) we classify as thermal emission. Emission that is spectrally narrow ($\geqslant 4\sigma$ in $\leqslant 4$ channels, 1.6 km s^{-1}) and spatially consistent with an unresolved point source we consider a candidate for maser emission. Within the category "maser," there are two subcategories. Emission spots classified as "maser" are candidate maser emission, and their highest flux density is in the 5_2 transition. Emission spots classified as "maser*" are likely to arise from non-thermal emission, but their highest flux density is in a transition other than 5_2 (usually 8_2). Figure 3 shows examples of maser and thermal spectra from our data.

The second method consisted of comparing our observed line ratios to line ratios produced by purely thermal, optically thin LTE emission. We numerically simulated line ratios for the optically thin LTE case and plotted these ratios (3_2:5_2, 8_2:5_2, and 10_2:5_2) for $T = 0$ K to $T = 300$ K. We then compared the observed line ratios for each fitted emission site to the simulated ratios. For lines with non-detections, we used an upper limit of 5σ in the ratio, where σ is the line rms from Table 2. Emission sites with line ratios inconsistent with LTE are candidates for maser emission. Ratios that match the simulated LTE emission indicate candidate thermal emission.

Our findings with the second method largely matched our classifications from the first method. We found only two exceptions to our original classifications: G12.91−0.03_b was classified as a maser, but its line ratios are consistent with optically thin LTE emission at lower temperatures ($\leqslant 40$ K). However, the T_B for the 5_2 emission is 82 K, far warmer than the temperature required to produce optically thin thermal emission. We therefore consider G12.91−0.03_b to be a maser. G22.04+0.22_b was classified as thermal emission based on its large fitted size, but its line ratios are potentially more consistent with maser emission. However, G22.04+0.22_b is in close proximity to G22.04+0.22_a ($\sim 1\farcs7$ and two channels), the strongest maser detected in our sample (7650 mJy in 5_2). The very strong emission from G22.04+0.22_a causes "ringing" in the surrounding channels, including those in which G22.04+0.22_b lies, so it is possible that the fitted flux densities of the 5_2 and 8_2 lines are skewed by this effect. It is also worth noting that G22.04+0.22_b would be the only 25 GHz maser in the sample without a 44 GHz counterpart, and that the 25 GHz CH_3OH emission is coincident with weak 1.3 cm emission (Table 4), increasing the chance of warm thermal gas at this location. Thus, we consider G22.04+0.22_b as most likely "thermal."

3.2.2. Detection Rates

Table 6 presents the number of 25 GHz CH_3OH detections in each transition by source, as well as the total number of maser and thermal emission spots for each EGO, and whether 1.3 cm continuum emission is detected associated with the EGO (within or touching the boundary of the extended 4.5 μm emission; Section 3.1). Emission from different transitions is co-spatial so, e.g., co-spatial emission in the 3_2, 5_2, and 8_2 lines would be counted as a single maser spot in column 7. We detected 25 GHz CH_3OH emission above the 4σ level in 16 of our 20 targets, for an overall detection rate of 80%. For the 25 GHz Class I CH_3OH masers, we found that the emission was strongest in the 5_2 transition (see Table 7), but that the 8_2 transition was not significantly weaker than the 5_2 transition in
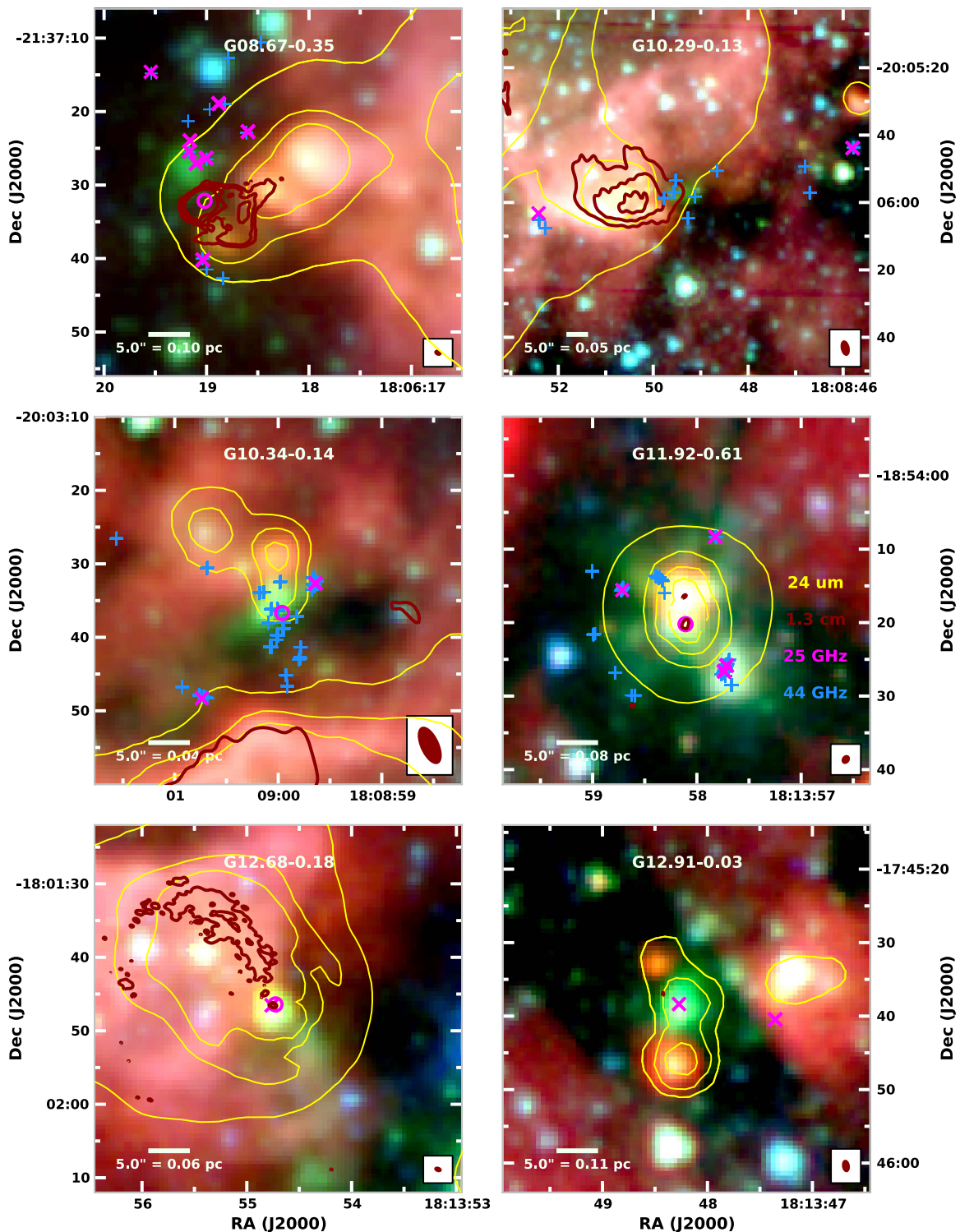
Figure 1. (a) *Spitzer* GLIMPSE three-color images (RGB: 8.0, 4.5, and 3.6 μm) for sources with detected 25 GHz CH$_3$OH emission. For each EGO, the displayed FOV is centered on the coordinates given in Table 2. *Spitzer* MIPSGAL 24 μm contours are overlaid in yellow (contour levels, in MJy sr^{-1}: G08.67: (300, 800, 1600); G10.29: (300, 1200, 1800); G10.34: (300, 900, 1300); G11.92: (300, 600, 1200, 1800); G12.68: (300, 900, 1300); G12.91: (300, 600, 1200); G14.33 (300, 1000, 1500, 2000); G14.63: (300, 600); G16.59: (300, 600, 1200); G18.67: (300, 900); G19.36: (300, 600, 1400); G22.04: (300, 900); G24.94: (300, 600, 900); G28.28: (300, 800, 1600); G35.03: (300, 900, 1300, 1700); G45.47: (300, 800, 1600)). VLA 1.3 cm continuum contours are overlaid in dark red (levels: 4, 12, 28, 60 × σ, where the σ for each field is given in Table 2). Sites of 25 GHz CH$_3$OH maser emission are marked by magenta × symbols, while sites of thermal 25 GHz CH$_3$OH emission are marked by magenta ○ symbols. Class I 44 GHz CH$_3$OH masers from the literature (where available) are marked with blue + symbols (see Table 1).

general (median flux densities of 58.5 and 52.0 mJy and median S/Ns of 18.6 and 13.2 for 5_2 and 8_2, respectively). In total, we fit 44 sites of CH$_3$OH emission. Of these 44 sites, we classified 10 as being purely thermal emission. Of the remaining 34 sites, we classified 30 as "maser" and 4 as "maser*" (as defined in Section 3.2.1). Detection rates and flux density statistics by transition and emission type are summarized in Table 7.
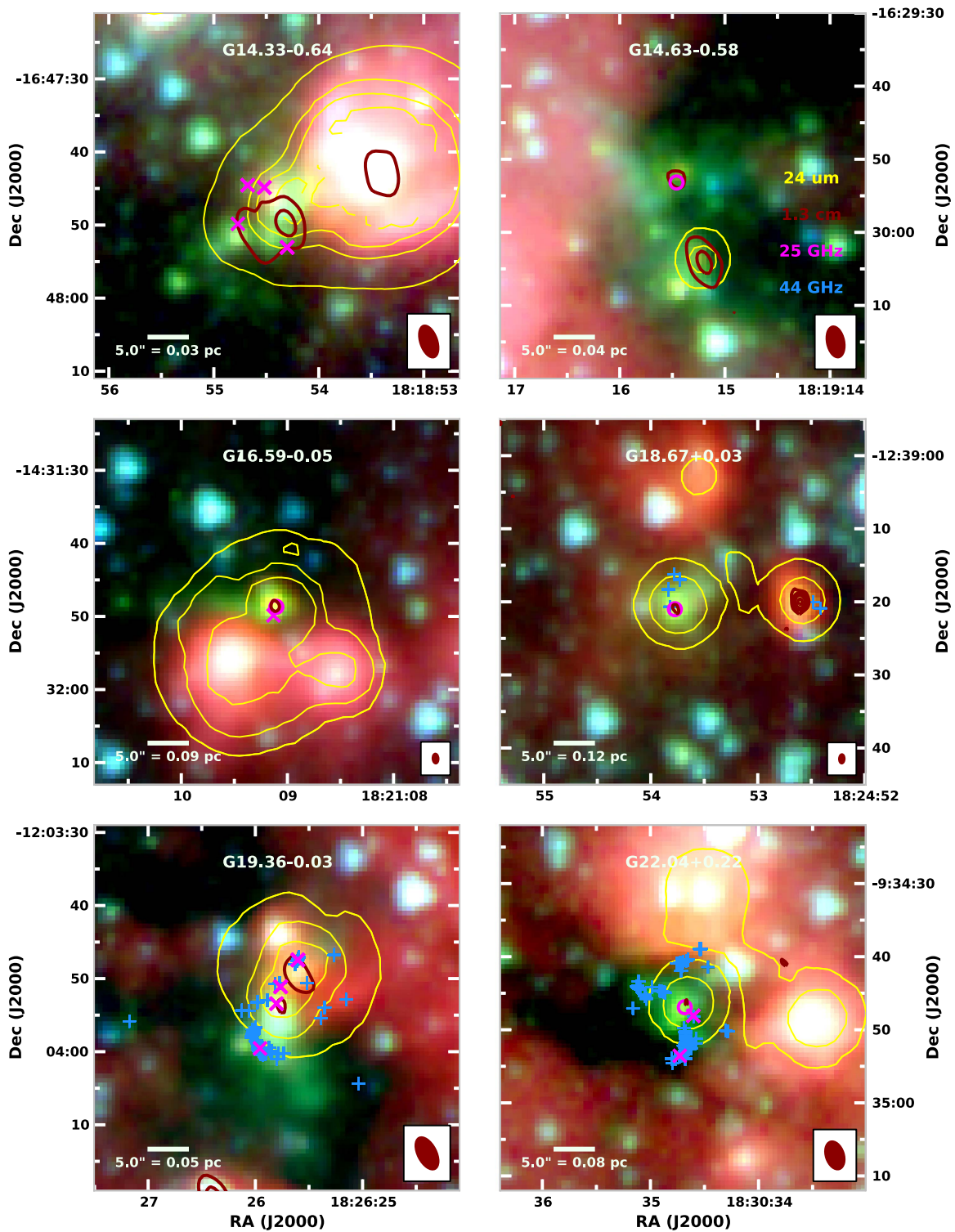
6

Figure 1. (Continued.)

Of the sites identified as thermal emission, one has emission only in the 5_2 line, one has emission only in the 3_2 and 5_2 lines, one has emission only in the 5_2 and 8_2 lines, and one has emission in the 3_2, 5_2, and 8_2 lines (Table 5). The remaining six sites have thermal emission in all four lines. For the source with thermal emission in 5_2 and 8_2 only (G18.67+0.03_a), we did identify weak thermal emission in the 3_2 line, but it is not above the 4σ level and so is not included in Table 5.

The 34 emission sites classified as "maser" or "maser*" have the following properties: 10 have emission above the 4σ level (where σ is the line rms from Table 2) in all four transitions (3_2, 5_2, 8_2, 10_2), including three of the four spots classified as "maser*"; eight have emission above the 4σ level in the 3_2, 5_2, and 8_2 lines only; two have emission above the 4σ level in the 5_2, 8_2, and 10_2 lines only; four have emission above the 4σ level in the 3_2 and 5_2 lines only; three have emission above the
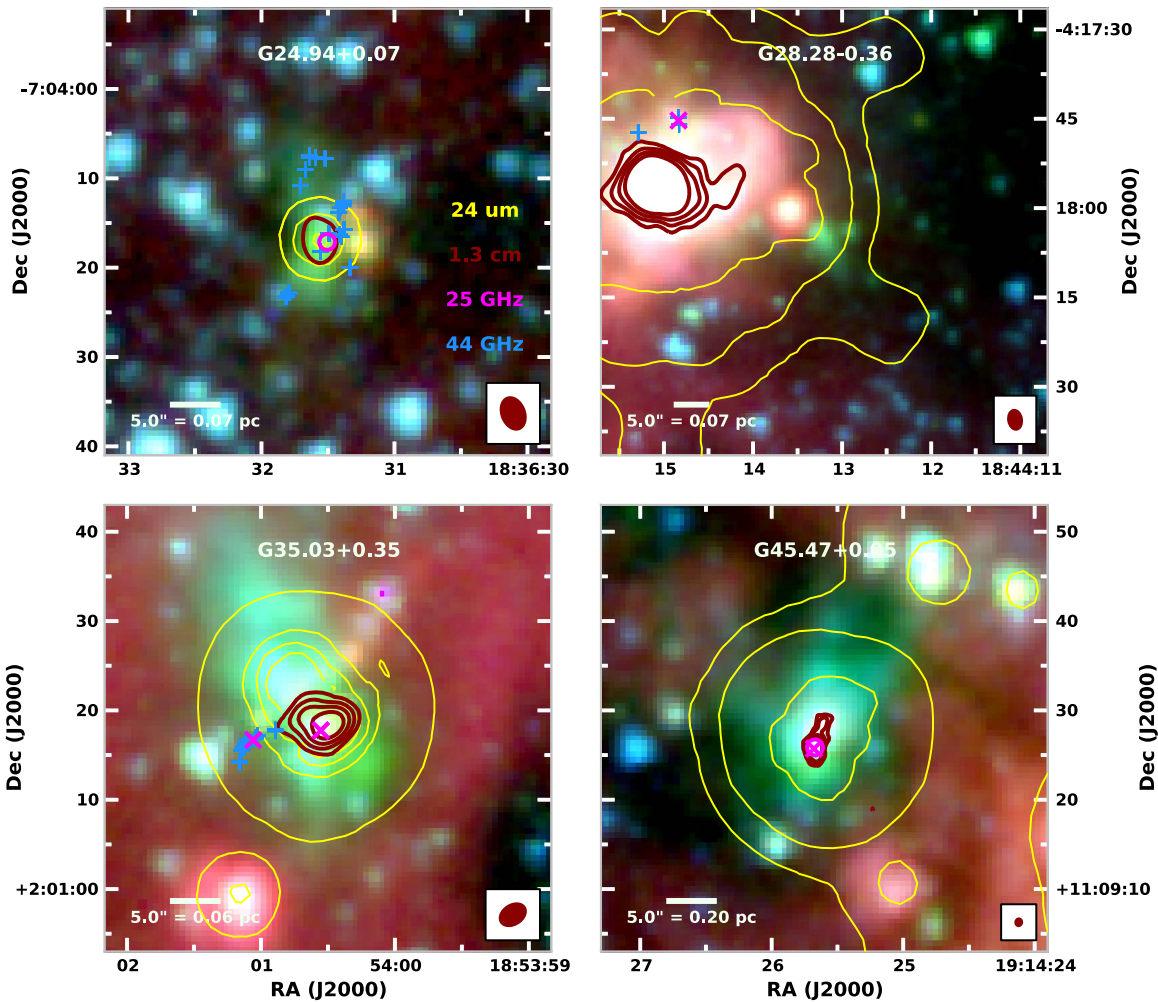
Figure 1. (Continued.)

4σ level in the 5_2 and 8_2 lines only; and seven have emission only in the 5_2 line. For this last group, the median and mean flux densities are 27.0 mJy and 35.9 mJy, respectively. These values are lower than the median and mean flux densities for the 5_2 population as a whole (see Table 7), but these masers are not the weakest masers in the overall population.

3.3. Notes on Individual Sources

The following subsections discuss each of the target EGOs for which we detect either 25 GHz CH$_3$OH or EGO-associated 1.3 cm continuum emission in greater detail, including notes on relevant high-resolution observations reported in the literature.

G08.67−0.35—We detect thermal 25 GHz CH$_3$OH in both emission and absorption (G08.67−0.35_d; see Figure 3) and resolved 1.3 cm continuum emission coincident with the known UCH II region G8.67−0.36 (Wood & Churchwell 1989). The northern edge of the UCH II region is coincident with the southern end of the extended 4.5 μm emission of the G08.67 −0.35 EGO (Figure 1). It is currently unclear whether the extended 4.5 μm emission arises from an outflow associated with the UCH II region or from an outflow driven by a less-evolved source that is (as yet) undetected in the 1.3 cm continuum. Four of the 25 GHz CH$_3$OH masers are coincident with the extended 4.5 μm emission, while three more lie in an arc 5″–8″ west and north of it. The thermal 25 GHz CH$_3$OH

emission is coincident with the UCH II region and with the Class II 6.7 GHz CH$_3$OH maser emission (G8.669−0.356) reported by Caswell (2009).

G10.29−0.13—Like Cyganowski et al. (2011a), we detect 1.3 cm continuum emission associated with the MIR-bright (MIPSGAL-saturated) source directly to the east of the EGO. Both the MIR-bright source and the EGO lie on the edge of the W31 H II region G10.32−00.15 (Westerhout 1958; see also the discussion in Cyganowski et al. 2011a). In our image, the 1.3 cm continuum emission partially overlaps the extended 4.5 μm emission of the EGO and so is included in Tables 4 and 6 as an EGO-associated 1.3 cm source (Section 3.1). We note, however, that the morphology of the 1.3 cm continuum differs markedly from that of the extended 4.5 μm emission, and it is unclear if the two are really associated. Indeed, Cyganowski et al. (2011a) deem their 1.3 and 3.6 cm detections to be unrelated (at the higher resolution and poorer sensitivity of those data, there is no overlap in the centimeter continuum and extended 4.5 μm emission). Higher angular resolution and sensitivity continuum observations are needed to verify that there is cm-λ emission directly associated with the EGO.

Unlike most EGOs, G10.29−0.13 lacks a discrete 24 μm counterpart, though it is associated with a 6.7 GHz Class II CH$_3$OH maser (Cyganowski et al. 2009). We do not detect any 25 GHz CH$_3$OH emission coincident with this EGO (Figure 1).
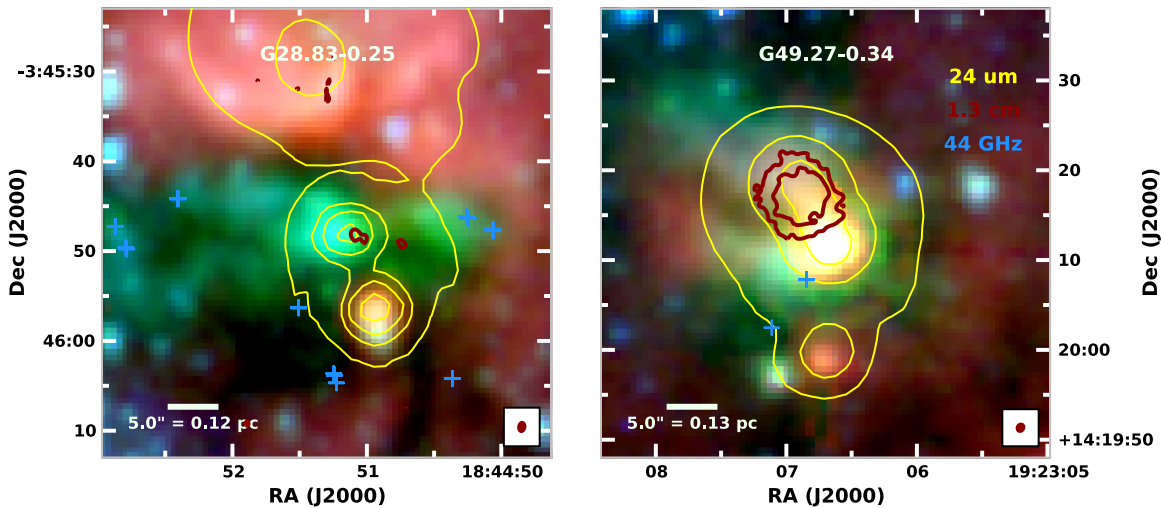
Figure 2. Same as Figure 1, but for sources with 1.3 cm continuum detections but no detected 25 GHz CH_3OH emission. MIPSGAL 24 μm contour levels are G28.83: 300, 900, 1300, 1700 MJy sr^{-1} and G49.27: 300, 800, 1600 MJy sr^{-1}.

We do detect two 25 GHz CH_3OH masers in the field, located $\sim25''$ NW and SE of the EGO, respectively, that appear to be distributed along the same line as the 44 GHz Class I CH_3OH masers reported in Cyganowski et al. (2009). Neither 25 GHz maser is associated with the 1.3 cm continuum or extended 4.5 μm emission.

G10.34−0.14—G10.34−0.14 is also located on the edge of the W31 H II region G10.32−00.15 (also see *G10.29−0.13*). We do not detect 1.3 cm continuum emission associated with the EGO. Within the VLA FOV, we detect extended 1.3 cm continuum emission from the nearby MIR-bright H II region and a weak, unresolved 1.3 cm source $\sim18''$ west of the EGO (Figure 1; not included in Table 4).

We detect 25 GHz thermal CH_3OH emission coincident with the EGO and with Class II 6.7 GHz CH_3OH maser emission (Cyganowski et al. 2009). The thermal CH_3OH emission is fairly extended, with a T_b of only 6 K (Table 5), and is coincident with the southern edge of an N–S elongated region of 24 μm emission. This MIR morphology may indicate the presence of two blended 24 μm sources. One 25 GHz CH_3OH maser is detected at the NW end of the extended 4.5 μm emission, coincident with a 44 GHz Class I CH_3OH maser reported by Cyganowski et al. (2009). The other 25 GHz maser is SE of the EGO, coincident with a separate patch of extended 4.5 μm emission and 44 GHz CH_3OH masers (Cyganowski et al. 2009).

G11.92−0.61—We detect three 1.3 cm continuum sources, two coincident with the EGO (CM1 and CM2, Table 4) and one at the SE edge of the extended 4.5 μm emission (Figure 1). The strongest 1.3 cm source, CM1 (previously reported by Cyganowski et al. 2011a, 2014; Ilee et al. 2016; Moscadelli et al. 2016), is coincident with the millimeter dust source and massive disk candidate MM1 (Cyganowski et al. 2011b; Ilee et al. 2016) and with the 6.7 GHz CH_3OH maser emission (Cyganowski et al. 2009). Based on modeling the centimeter–submillimeter spectral energy distribution (SED) of MM1, Ilee et al. (2016) argue that its cm-λ emission is attributable to free–free emission from a gravitationally trapped hypercompact (HC) H II region, with a possible contribution from a compact ionized jet (see also Moscadelli et al. 2016). We detect 25 GHz thermal CH_3OH emission coincident with CM1, consistent with the classification of MM1 as a hot core based on

inteferometric (sub)millimeter line observations (Cyganowski et al. 2011b, 2014; Ilee et al. 2016).

Located $\sim3''$ north of CM1, CM2 is also coincident with 6.7 GHz Class II CH_3OH maser emission (Cyganowski et al. 2009). This weak, unresolved 1.3 cm source (~0.3 mJy beam^{-1}, Table 4) is the cm-λ counterpart of the millimeter source MM3 −C1 (Cyganowski et al. 2011b, 2017) and was detected at 0.9 and 3 cm with the VLA by Cyganowski et al. (2017). The third 1.3 cm source is $\sim13''$ SE of CM1, toward the edge of the extended 4.5 μm emission. This centimeter detection is weak and unresolved, and is not associated with compact 24 μm or (sub) millimeter emission. It is located within $1''$ of a 44 GHz Class I CH_3OH maser (Cyganowski et al. 2009), but the relationship between the maser and the centimeter emission is unclear.

We detect four 25 GHz CH_3OH masers in this target, all of which have 44 GHz CH_3OH maser counterparts. These masers are all located toward the edges of the extended 4.5 μm emission and are distinctly separated ($>5''$) from the centimeter emission and MIPSGAL 24 μm peak.

G12.68−0.18—We detect a compact 1.3 cm continuum source coincident with the EGO, as well as extended ($>15''$) 1.3 cm emission coincident with similarly extended MIPSGAL 24 μm emission. The EGO-related centimeter source, which we denote CM1, was studied by Moscadelli et al. (2016) with the VLA. Based on their high-resolution multiwavelength observations (resolution $\lesssim0.''3$ at 4.8, 2.3, and 1.4 cm), Moscadelli et al. (2016) suggest that the cm-λ continuum emission arises from an ionized jet.

CM1 is coincident with both thermal and masing 25 GHz CH_3OH emission (Figure 1), and with a 6.7 GHz Class II CH_3OH maser (Caswell 2009; see also discussion in Moscadelli et al. 2016). The 25 GHz thermal emission has a brightness temperature of 90 K, suggestive of warm gas on small size scales. This is consistent with the results from Submillimeter Array (SMA) observations of the W33 complex by Immer et al. (2014), who find that the millimeter continuum counterpart to CM1 (W33B; see their Figure 6) is a hot core rich in nitrogen-bearing species, with gas temperatures of ~220–350 K.

G12.91−0.03—We detect one weak, unresolved 1.3 cm continuum source and two 25 GHz CH_3OH masers in the VLA FOV. The 1.3 cm source, which we denote CM1, is located at

Table 4
1.3 cm Continuum Flux Densities for Emission Associated with EGO Targets

Source Name	J2000 Coordinates α(h m s)	δ(° ′ ″)	Peak Intensity (mJy beam^{-1})	Integrated[a] (mJy)	Prior 1.3 cm Detections?	References[b]	Prior cm-λ Detections?	References
G08.67−0.35_CM1	18:06:19.01	−21:37:32.2	183.0 (0.1)	1141 (1)	N	–	Y	W89
G10.29−0.14_CM1	18:08:50.47	−20:06:01.5	10.7 (0.3)	201 (2)	Y	C11b[c]	Y	C11b[c]
G11.92−0.64_CM1	18:13:58.108 (0.003)	−18:54:20.212 (0.09)	0.62 (0.08)	unr	Y	C11b	Y	M16
_CM2	18:13:58.121 (0.009)	−18:54:16.46 (0.13)	0.32 (0.07)	unr	N	–	Y	C17
G12.68−0.18_CM1	18:13:54.750 (0.002)	−18:01:46.52 (0.01)	0.73 (0.06)	unr	Y	M16	Y	M16
G12.91−0.03_CM1	18:13:48.41 (0.01)	−17:45:36.92 (0.2)	0.23 (0.05)	unr	N	–	N	–
G14.33−0.64_CM1	18:18:54.30	−16:47:50.0	1.78 (0.1)	4.1 (0.3)	N	–	N	–
G14.63−0.58_CM1	18:19:15.19	−16:30:04.0	0.99 (0.06)	1.2 (0.1)	N	–	N	–
_CM2	18:19:15.469 (0.03)	−16:29:52.4 (0.4)	0.29 (0.07)	unr	N	–	N	–
G16.59−0.05_CM1	18:21:09.116 (0.004)	−14:31:48.58 (0.08)	0.56 (0.07)	unr	Y	R16, H11[d], Z06	Y	M16, R16, Z06
G18.67+0.03_CM1	18:24:53.755 (0.007)	−12:39:20.9 (0.2)	0.18 (0.04)	unr	N	–	N	–
G19.36−0.03_CM1	18:26:25.60 (0.02)	−12:03:49.6 (0.4)	0.7 (0.1)	1.3 (0.3)	N	–	Y	C11b[e]
_CM2	18:26:25.77 (0.01)	−12:03:53.7 (0.5)	0.5 (0.1)	unr	N	–	N	–
G22.04+0.22_CM1	18:30:34.70 (0.03)	−09:34:46.2 (0.5)	0.6 (0.1)	unr	N	–	N	–
G24.94+0.07_CM1	18:36:31.563 (0.008)	−07:04:16.8 (0.2)	0.85 (0.09)	unr	N	–	Y	C11b
G28.83−0.25_CM1	18:44:50.74 (0.01)	−03:45:49.19 (0.08)	0.24 (0.04)	unr	N	–	Y	C11b
_CM2	18:44:51.086 (0.005)	−03:45:48.22 (0.08)	0.35 (0.05)	unr	N	–	Y	C11b
G35.03−0.03_CM1	18:54:00.50	+02:01:18.5	13.9 (0.1)	18.5 (0.3)	Y	B11, C11b[f]	Y	C11b
G45.47+0.05_CM1	19:14:25.68	+11:09:25.8	110.09 (0.09)	180.9 (0.4)	Y	H99	Y	W89
G49.27−0.34_CM1	19:23:06.87	+14:20:18.2	1.62 (0.07)	57.8 (0.6)	Y	C11b	Y	C11b

Notes.

[a] Flux densities with reported values were measured within the 3σ contour; see Table 2 for σ values. In this case, the position is that of the peak pixel within the 3σ contour. Flux densities designated by "unr" indicate that the emission is unresolved. For these cases, the Gaussian fitted position and peak intensity along with the statistical uncertainties are reported.

[b] Reference abbreviations correspond to B11: Brogan et al. (2011), C11b: Cyganowski et al. (2011a), C17: Cyganowski et al. (2017), H99: Hofner et al. (1999), H11: Hofner et al. (2011), M16: Moscadelli et al. (2016), R16: Rosero et al. (2016), W89: Wood & Churchwell (1989), Z06: Zapata et al. (2006).

[c] Cyganowski et al. (2011a) list this as a field source, designation F-CM1.

[d] Hofner et al. (2011) list this source as IRAS 18182-1433, Component B.

[e] Cyganowski et al. (2011a) list this is a field source, designation F-CM1.

[f] G35.03−0.03_CM1 from the current work is a blend of CM1, CM2, CM4, and CM5 from Cyganowski et al. (2011a).

Table 5
25 GHz CH$_3$OH Emission: Fitted and Derived Properties

Emission Region	Fitted Position (J2000) R.A. (h m s)	Decl. (° ′ ″)	V_{peak}[c] (km s^{-1})	V_{range}[d] (km s^{-1})	Fitted Size[a] Major × Minor [PA] (″) × (″) [°]	3$_2$ Flux (mJy)	5$_2$ Flux (mJy)	8$_2$ Flux (mJy)	10$_2$ Flux (mJy)	5$_2$ T_B (K)	Emission Type[e]
G08.67−0.35_a	18:06:18.596 (0.005)	−21:37:22.72 (0.09)	38.2	37.0–39.0	0.72 × <0.69 (0.27)	–	10 (3)	–	–	40	Maser
G08.67−0.35_b	18:06:18.881 (0.002)	−21:37:18.90 (0.02)	38.2	37.4–39.0	<0.69	–	13 (2)	5 (1)	–	52	Maser
G08.67−0.35_c	18:06:19.003 (0.001)	−21:37:26.34 (0.01)	35.0	34.2–35.8	0.39 × <0.69 (0.09)	18 (3)	44 (2)	6 (1)	–	320	Maser
G08.67−0.35_d	18:06:19.019 (0.004)	−21:37:32.15 (0.05)	36.2	35.4–39.0	1.63 × 1.41 [80] (0.18 × 0.16 [77])	120 (10)	130 (10)	63 (6)	40 (7)	110	Thermal+Abs
G08.67−0.35_e	18:06:19.036 (0.001)	−21:37:40.18 (0.01)	33.4	32.6–34.6	0.27 × <0.34* (0.06)	23 (5)	99 (3)	31 (2)	–	2110	Maser
G08.67−0.35_f	18:06:19.101 (0.002)	−21:37:27.05 (0.02)	36.2	35.8–37.0	0.40 × <0.69 (0.15)	–	23 (3)	15 (2)	–	165	Maser
G08.67−0.35_g	18:06:19.162 (0.001)	−21:37:23.95 (0.10)	35.4	35.0–36.6	<0.69	–	28 (2)	–	–	116	Maser
G08.67−0.35_h	18:06:19.168 (0.0001)	−21:37:25.427 (0.002)	35.8	34.2–37.4	0.15 × 0.10 (0.05 × 0.04) [35 (45)]	106 (4)	791 (9)	91 (3)	14 (4)	104000	Maser
G08.67−0.35_i	18:06:19.544 (0.001)	−21:37:14.60 (0.01)	36.6	35.8–37.4	<0.69	–	27 (2)	–	–	113	Maser
G10.29−0.13_a	18:08:45.802 (0.001)	−20:05:43.85 (0.04)	14.6	13.8–15.0	1.31 × <1.64* (0.37)	41 (9)	288 (7)	97 (5)	–	263	Maser
G10.29−0.13_b	18:08:52.416 (0.003)	−20:06:03.20 (0.10)	15.4	15.0–16.6	<3.28	–	97 (7)	60 (10)	–	18	Maser
G10.34−0.14_a	18:08:59.640 (0.0002)	−20:03:32.661 (0.01)	14.8	14.0–15.6	1.32 × 0.50 [34.8] (0.08 × 0.05 [3.3])	1058 (9)	2760 (10)	766 (6)	–	8200	Maser
G10.34−0.14_b	18:08:59.963 (0.022)	−20:03:36.68 (0.39)	12.8	9.2–13.6	5.29 × <2.51 (1.78)	30 (6)	41 (7)	37 (7)	–	6	Thermal
G10.34−0.14_c	18:09:00.738 (0.014)	−20:03:48.30 (0.42)	11.6	11.2–12.4	<3.60	14 (3)	36 (5)	–	–	5.4	Maser
G11.92−0.61_a	18:13:57.715 (0.0001)	−18:54:25.836 (0.01)	34.0	32.8–34.4	0.50 × 0.16 [154] (0.04 × 0.07 [5])	150 (3)	511 (6)	19 (5)	–	12500	Maser
G11.92−0.61_b	18:13:57.739 (0.001)	−18:54:26.64 (0.02)	35.2	34.8–35.6	0.55 × <1.06 (0.14)	18 (3)	35 (2)	–	–	116	Maser
G11.92−0.61_c	18:13:57.824 (0.002)	−18:54:08.30 (0.11)	36.4	35.6–37.2	1.53 × <1.06 (0.38)	–	18 (3)	–	–	22	Maser
G11.92−0.61_d	18:13:58.109 (0.007)	−18:54:20.21 (0.19)	36.8	33.6–40.0	3.71 × 2.01 [9] (0.50 × 0.27 [9])	80 (10)	54 (7)	41 (6)	42 (7)	14	Thermal
G11.92−0.61_e	18:13:58.715 (0.002)	−18:54:15.57 (0.06)	36.8	36.4–37.2	1.13 × 0.59 [153] (0.25 × 0.22 [22])	22 (2)	18 (2)	–	–	53	Maser
G12.68−0.18_a	18:13:54.726 (0.003)	−18:01:46.41 (0.02)	56.0	53.2–59.2	1.06 × 0.69 [90] (0.14 × 0.10 [17])	24 (4)	33 (3)	39 (3)	43 (4)	90	Thermal
G12.68−0.18_b	18:13:54.763 (0.002)	−18:01:46.54 (0.05)	52.4	52.0–52.8	0.91 × 0.28 [174] (0.18 × 0.29 [18])	–	18 (2)	13 (2)	19 (3)	140	Maser*
G12.91−0.03_a	18:13:47.355 (0.001)	−17:45:40.46 (0.05)	55.0	54.2–56.2	<1.12	–	23 (3)	–	–	36	Maser
G12.91−0.03_b	18:13:48.271 (0.001)	−17:45:38.36 (0.04)	57.8	56.6–60.2	1.25 × <1.12 (0.15)	50 (20)	59 (3)	27 (3)	–	82	Maser
G14.33−0.64_a	18:18:54.302 (0.006)	−16:47:53.06 (0.16)	21.6	20.8–21.6	3.24 × 2.52 [7] (0.73 × 0.56 [88])	–	99 (8)	–	–	24	Maser
G14.33−0.64_b	18:18:54.519 (0.002)	−16:47:44.86 (0.04)	20.4	20.0–21.2	1.56 × 1.13 [47] (0.36 × 0.40 [45])	50 (10)	400 (10)	362 (7)	96 (5)	447	Maser
G14.33−0.64_c	18:18:54.678 (0.007)	−16:47:44.54 (0.14)	22.4	22.0–23.2	<2.87	8 (2)	41 (4)	31 (2)	–	7.1	Maser
G14.33−0.64_d	18:18:54.771 (0.007)	−16:47:49.84 (0.11)	22.8	22.4–23.2	3.18 × <2.45 (0.32)	31 (6)	58 (3)	52 (5)	13 (2)	14.6	Maser
G14.63−0.58_a	18:19:15.46 (0.01)	−16:29:53.18 (0.32)	19.4	19.4–19.8	5.07 × <2.50 (1.11) [14]	27 (5)	19 (3)	–	–	2.9	Thermal
G16.59−0.05_a	18:21:09.104 (0.002)	−14:31:48.69 (0.07)	58.6	57.0–59.8	1.68 × 0.96 [167] (0.24 × 0.14 [12])	25 (4)	36 (3)	27 (3)	19 (3)	44	Thermal
G16.59−0.05_b	18:21:09.131 (0.0003)	−14:31:49.860 (0.01)	61.4	61.0–61.8	0.40 × 0.22 [178] (0.08 × 0.05 [19])	16 (3)	320 (6)	205 (4)	29 (4)	7200	Maser
G18.67+0.03_a	18:24:53.775 (0.005)	−12:39:21.01 (0.15)	78.2	78.2–79.4	1.68 × 0.91 [165] (0.51 × 0.34 [37])	–	12 (2)	6 (1)	–	15	Thermal
G19.36−0.03_a	18:26:25.604 (0.001)	−12:03:47.44 (0.03)	26.0	25.6–26.4	<1.75*	60 (10)	130 (3)	–	–	84	Maser
G19.36−0.03_b	18:26:25.765 (0.002)	−12:03:51.113 (0.05)	26.4	25.2–26.8	<3.51	29 (3)	91 (4)	117 (2)	38 (1)	14.4	Maser*
G19.36−0.03_c	18:26:25.803 (0.003)	−12:03:53.43 (0.16)	27.6	27.6–28.0	<3.51	–	46 (2)	–	–	7.4	Maser
G19.36−0.03_d	18:26:25.957 (0.0002)	−12:03:59.547 (0.01)	26.4	24.4–28.4	1.31 × 0.52 [30] (0.05 × 0.03 [2])	2870 (10)	6390 (20)	1370 (10)	135 (6)	18420	Maser
G22.04+0.22_a	18:30:34.603 (0.0002)	−09:34:48.087 (0.01)	51.8	51.0–55.0	<1.63*	1090 (10)	7650 (30)	3920 (10)	723 (6)	5660	Maser
G22.04+0.22_b	18:30:34.682 (0.005)	−09:34:46.91 (0.13)	50.2	47.8–50.6	2.71 × 1.70 [23] (0.58 × 0.39 [34])	70 (10)	200 (20)	160 (5)	70 (4)	86	Thermal
G22.04+0.22_c	18:30:34.729 (0.001)	−09:34:53.56 (0.02)	50.2	49.4–50.6	0.69 × <1.63* (0.30)	48 (4)	342 (7)	47 (7)	–	598	Maser

Table 5
(Continued)

Emission Region	Fitted Position (J2000)		V_{peak}[c] (km s^{-1})	V_{range}[d] (km s^{-1})	Fitted Size[a]	Fitted Flux Densities[b]				5_2 T_B (K)	Emission Type[e]
	R.A. (^{h} ^{m} ^{s})	Decl. (° $'$ $''$)			Major × Minor [PA] ($''$) × ($''$) [°]	3_2 Flux (mJy)	5_2 Flux (mJy)	8_2 Flux (mJy)	10_2 Flux (mJy)		
G24.94+0.07_a	18:36:31.506 (0.010)	−07:04:17.12 (0.43)	42.2	39.0–45.0	<3.36	–	11 (3)	–	–	2.0	Thermal
G28.28−0.36_a	18:44:14.836 (0.003)	−04:17:45.29 (0.09)	48.2	47.4–49.0	1.87 × <2.72 (0.48)	20 (5)	93 (7)	70 (7)	40 (10)	36	Maser
G35.03+0.35_a	18:54:00.554 (0.001)	+02:01:17.75 (0.07)	54.8	54.4–55.2	<3.25	–	19 (2)	48 (1)	18 (2)	3.6	Maser*
G35.03+0.35_b	18:54:01.058 (0.005)	+02:01:16.69 (0.01)	52.8	52.0–53.6	<1.63*	23 (4)	252 (3)	130 (4)	15 (5)	186	Maser
G45.47+0.05_a	19:14:25.671 (0.007)	+11:09:25.86 (0.10)	64.4	63.2–64.8	1.61 × <0.90 (0.37)	11 (2)	18 (4)	17 (2)	23 (5)	24	Thermal
G45.47+0.05_b	19:14:25.679 (0.001)	+11:09:25.71 (0.02)	66.4	65.2–67.2	<0.90	13 (2)	21 (1)	41 (1)	39 (2)	51	Maser*

Notes.

[a] For sources for which the fitted size is poorly constrained (fitted size <2× the statistical uncertainty from `imfit`) and the S/N < 50, we report the geometric mean of the synthesized beam as an upper limit on the source size (indicated with "<"). For sources for which the fitted size is poorly constrained (fitted size <2× the statistical uncertainty from `imfit`) and the S/N > 50, we report half the geometric mean of the synthesized beam as an upper limit on the source size (indicated with "<" and a "*" after the value.)

[b] Dashes indicate non-detections (no emission above 4σ). The upper limits in these cases should be taken as four times the line rms from Table 2.

[c] Velocity of the peak emission in the 5_2 line.

[d] Velocity range over which emission was detected at the ⩾4σ level and `imfit` was run.

[e] Classification of emission as "thermal" or "maser," as described in Section 3.2.1. Sources denoted "maser*" are maser (non-thermal) emission, but their maximum fitted flux density occurs in a line higher than 5_2.
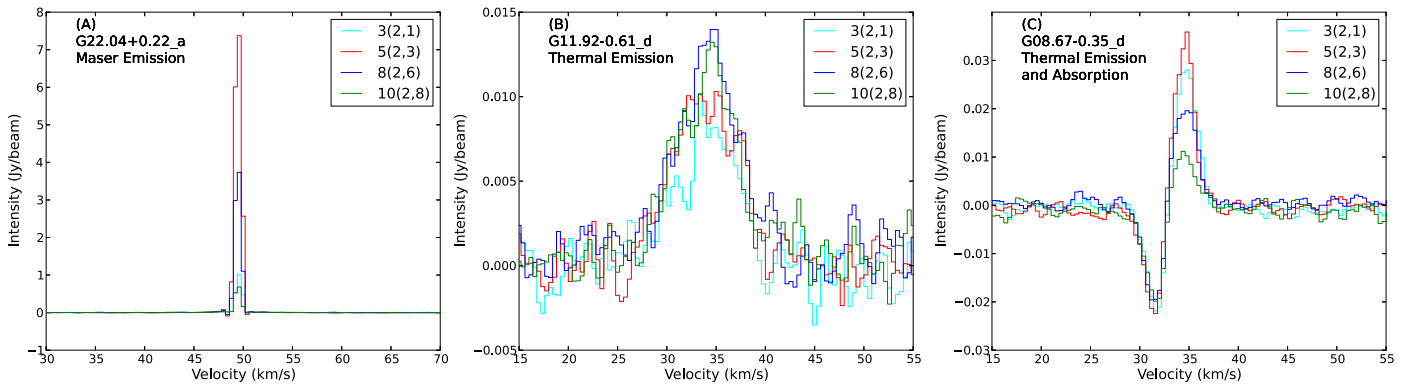
Figure 3. Example spectra for the two categories of emission (maser and thermal), as well as a spectrum showing both thermal absorption and emission. All three sets of spectra span 40 km s^{-1}.

the NE edge of the extended 4.5 μm emission (Figure 1). One of the 25 GHz masers is coincident with the extended 4.5 μm emission, 24 μm emission, and the 6.7 GHz Class II CH$_3$OH maser G12.904-0.031 (Green et al. 2010). The second 25 GHz maser is located just beyond the western edge of the extended 4.5 μm emission, toward the edge of a more evolved, 8 μm bright region.

G14.33−0.64—This EGO is located $\sim$15″ SE of the bright far-infrared source IRAS 18159-1648 (Jaffe et al. 1982), within a ridge of ammonia emission (VLA observations by Lu et al. 2014). We detect marginally resolved 1.3 cm continuum emission coincident with the EGO (denoted CM1) and also the IRAS source (Figure 1). The morphology of CM1 is consistent with two unresolved cm-λ continuum sources. Both components have emission above 6σ, but satisfactory two-component fits could not be achieved with the current data.

We detect four 25 GHz CH$_3$OH masers and no thermal CH$_3$OH emission in this source. The 25 GHz CH$_3$OH emission is, however, confused both spatially and spectrally. Consequently, there may be additional weak CH$_3$OH emission present that could not be separated in the current data. Two of the 25 GHz masers are located just within the 4σ contour of the 1.3 cm continuum emission; two are located north of the centimeter source.

G14.63−0.58—We detect two 1.3 cm continuum sources, both coincident with extended 4.5 μm emission (Figure 1). The brighter centimeter source, CM1, is also coincident with compact 24 μm emission and with the 6.7 GHz CH$_3$OH maser G14.631−0.577, reported by Green et al. (2010). Thermal 25 GHz CH$_3$OH emission is detected toward CM2, the weaker centimeter continuum source. The brightness temperature of this thermal CH$_3$OH emission is only $T_b = 2.9$ K, due to the extended nature of the emission and consequent large fitted size; our optically thin calculation method gives a temperature range of $T = 10$–40 K. No 25 GHz CH$_3$OH masers are detected in the field.

G16.59−0.05—This EGO is adjacent to IRAS 18182−1433 (nominal separation $\sim$19″; Cyganowski et al. 2008); unusually among our sample, its cm-λ continuum emission has been well studied, primarily by authors targeting the IRAS source (e.g., Zapata et al. 2006; Sanna et al. 2010; Hofner et al. 2011; Moscadelli et al. 2013, 2016; Rosero et al. 2016). We detect a single compact 1.3 cm continuum source (CM1), which is coincident with the EGO and with a local peak in the 24 μm emission (Figure 1). CM1 corresponds to the brightest of the five components (18182-1433 C) detected at both 1.3 cm and

6 cm in deep VLA observations of this field by Rosero et al. (2016), who measure a spectral index of +0.8 ± 0.1 for this object. The compact 1.3 cm source is coincident with the 6.7 GHz CH$_3$OH maser emission (e.g., Green et al. 2010; Sanna et al. 2010; Moscadelli et al. 2013). At longer wavelengths, the continuum emission is elongated E–W, with a size scale of $\sim$4″ at 6 cm (Moscadelli et al. 2013, 2016). The orientation of this elongation, which is interpreted as an ionized jet (e.g., Moscadelli et al. 2013, 2016), is notably similar to that of the extended 4.5 μm emission of the EGO, which is elongated E–W on larger scales ($\sim$10″–15″).

We detect thermal 25 GHz CH$_3$OH emission that is coincident with the EGO and CM1, and with the 6.7 GHz CH$_3$OH maser G16.585−0.051 reported by Green et al. (2010). The detection of thermal CH$_3$OH at 25 GHz is consistent with the identification of this source as a hot core by Beuther et al. (2006) using SMA observations and by Lu et al. (2014) using VLA observations. We also detect one 25 GHz maser, located $<$1″ S–SE of the thermal CH$_3$OH emission.

G18.67+0.03—We detect two sources of 1.3 cm continuum emission in the VLA FOV (Figure 1). CM1 is weak, unresolved, and coincident with the EGO, a compact MIPSGAL 24 μm source, and 6.7 GHz Class II CH$_3$OH maser emission (Cyganowski et al. 2009; Green et al. 2010; see also Cyganowski et al. 2012). The measured peak intensity of CM1 (0.18 mJy beam^{-1}, Table 4) is consistent with this source being undetected by Cyganowski et al. (2011a; 4σ upper limit of 0.94 mJy beam^{-1} at 1.3 cm). We also detect strong, resolved 1.3 cm continuum emission $\sim$13″ W of the EGO, from the source designated "UCHII" by Cyganowski et al. (2012; F G18.67+0.03-CM1 in Cyganowski et al. 2011a).

The only 25 GHz CH$_3$OH detection in the field is thermal, and is coincident with CM1 and 6.7 GHz CH$_3$OH maser emission. Unusually, CH$_3$OH emission is detected in the 5$_2$ and 8$_2$ lines, but not 3$_2$. The brightness temperature $T_b = 15$ K, with the optically thin LTE calculations suggesting a temperature range of 40–50 K. The detection of thermal CH$_3$OH at 25 GHz is consistent with the presence of strong hot core molecular line emission from the EGO in SMA observations by Cyganowski et al. (2012), who find a CH$_3$CN temperature of 175 K. Notably, though both the EGO and the UC H II region to the west are associated with 44 GHz Class I CH$_3$OH masers (Cyganowski et al. 2009, 2012), no 25 GHz CH$_3$OH maser emission is detected within the VLA FOV.

G18.89−0.47—No 1.3 cm continuum or 25 GHz CH$_3$OH line emission was detected toward this EGO.

Table 6
25 GHz CH$_3$OH Emission Statistics by Target

Source Name	25 GHz Emission	Total 25 GHz Detections				Maser Emission	Thermal Emission	1.3 cm EGO Continuum
		3_2	5_2	8_2	10_2			
G08.67−0.35	Y	4	9	6	2	8	1	Y
G10.29−0.13	Y	1	2	2	0	2	0	Y
G10.34−0.14	Y	3	3	2	0	2	1	N
G11.92−0.61	Y	4	5	2	1	4	1	Y
G12.68−0.18	Y	1	2	2	2	1	1	Y
G12.91−0.03	Y	1	2	1	0	2	0	Y
G14.33−0.64	Y	3	4	3	2	4	0	Y
G14.63−0.58	Y	1	1	0	0	0	1	Y
G16.59−0.05	Y	2	2	2	2	1	1	Y
G18.67+0.03	Y	0	1	1	0	0	1	Y
G18.89−0.47	N	0	0	0	0	0	0	N
G19.36−0.03	Y	3	4	2	2	4	0	Y
G22.04+0.22	Y	3	3	3	2	2	1	Y
G24.94+0.07	Y	0	1	0	0	0	1	Y
G25.27−0.43	N	0	0	0	0	0	0	N
G28.28−0.36	Y	1	1	1	1	1	0	N
G28.83−0.25	N	0	0	0	0	0	0	Y
G35.03+0.35	Y	1	2	2	2	2	0	Y
G45.47+0.05	Y	2	2	2	2	1	1	Y
G49.27−0.34	N	0	0	0	0	0	0	Y

G19.36−0.03—We detect three sources of 1.3 cm continuum emission in the field, two of which (CM1 and CM2) are associated with MIPSGAL 24 μm emission (Figure 1). The 24 μm emission is elongated (NW–SE); its morphology suggests at least two components, separated by ∼6″. The weak 1.3 cm source CM1 (1.3 mJy, Table 4) is associated with the NW 24 μm component and coincides with the previously detected 3.6 cm source denoted F-CM1 by Cyganowski et al. (2011a).

CM2 is a new cm-λ detection and is coincident with the EGO and with Class II 6.7 GHz CH$_3$OH maser emission (Cyganowski et al. 2009). CM2 is unresolved and weak (0.40 mJy, Table 4), consistent with the previous 4σ upper limit of 1 mJy at 1.3 cm (Cyganowski et al. 2011a). The third 1.3 cm continuum source lies partially off the southern edge of the field shown in Figure 1, and was also detected by Cyganowski et al. (2011a) at 3.6 cm (their F-CM2).

We detect four 25 GHz Class I CH$_3$OH masers in this field, all of which have 44 GHz counterparts. The masers lie approximately along a line connecting the northern edge of CM1 and an arc of 44 GHz CH$_3$OH masers to the SW, including one that is near CM2.

G22.04+0.22—We detect two 1.3 cm continuum sources in the field. CM1 is a weak (0.6 mJy beam^{-1}, Table 4), unresolved source that is coincident with the EGO, compact 24 μm emission, and 6.7 GHz CH$_3$OH masers (Cyganowski et al. 2009). A second centimeter continuum source is detected ∼15″ NW of the EGO and does not appear to be associated. Neither centimeter continuum source was detected by Cyganowski et al. (2011a), consistent with their 4σ upper limit of 1 mJy at 1.3 cm.

We detect thermal 25 GHz CH$_3$OH emission coincident with CM1 and the 6.7 GHz masers (Figure 1). We also detect two 25 GHz CH$_3$OH masers, one of which is <2″ SW of CM1 and its thermal 25 GHz CH$_3$OH emission. The second 25 GHz maser is coincident with a line of 44 GHz CH$_3$OH masers that extends to the south of the EGO (Cyganowski et al. 2009).

G24.94+0.07—We detect weak 1.3 cm continuum emission coincident with this EGO (0.85 mJy beam^{-1}, Table 4). The 1.3 cm source, CM1, is coincident with compact MIPSGAL 24 μm emission and 6.7 GHz CH$_3$OH masers (Cyganowski et al. 2009). CM1 was detected by Cyganowski et al. (2011a) at 3.6 cm (peak intensity 0.53 ± 0.04 mJy beam^{-1}); our 1.3 cm detection is consistent with their 4σ upper limit of 1.0 mJy at 1.3 cm. Unfortunately, the mismatch in beam size between the 3.6 and 1.3 cm detections precludes analysis of the centimeter-wavelength SED. The only 25 GHz CH$_3$OH emission detected in this source is the thermal emission associated with CM1 (Figure 1).

G25.27−0.43—No 1.3 cm continuum emission is detected toward this EGO. An evolved H II region located ∼30″ SE of the EGO is detected in the 1.3 cm continuum; this source was detected by Cyganowski et al. (2011a) at 3.6 cm, who designated it F-CM2. No 25 GHz CH$_3$OH emission was detected within the VLA FOV.

G28.28−0.36—The only 1.3 cm continuum emission detected in this field is strong, resolved emission associated with the well-known core-halo UC H II region G28.288–0.364 (e.g., Kurtz et al. 1994), ∼20″ E–NE of the EGO (Figure 1). This UC H II region was detected at 3.6 and 1.3 cm by Cyganowski et al. (2011a), who designated it F-CM1. Notably, we do not detect 1.3 cm continuum emission from the Cyganowski et al. (2011a) 3.6 cm source CM1, which is coincident with the EGO and ∼1″.2 NE of a 6.7 GHz CH$_3$OH maser (Cyganowski et al. 2009, 2011a). The relatively high rms noise of the new 1.3 cm VLA image for this source (the third highest of our sample; Table 2) means that our 1.3 cm limit is only a factor of ∼1.4 improvement over that of Cyganowski et al. (2011a), and the mismatch in beam size precludes combining the two data sets to better constrain CM1's cm-λ spectral index. Only one 25 GHz CH$_3$OH maser is detected within the VLA FOV; this maser is ∼7″ north of F-CM1 and is coincident with a 44 GHz CH$_3$OH maser reported by Cyganowski et al. (2009).

Table 7
25 GHz CH$_3$OH Emission Statistics by Transition

Transition	Detection Rate	Median Flux Density (mJy)	Mean Flux Density (mJy)	Median S$_{peak}$/N	Mean S$_{peak}$/N
		Maser Detection Statistics			
3(2,1)–3(1,2)	60% (12/20)	30.0	261.7	7.8	47.4
5(2,3)–5(1,4)	80% (13/20)	58.5	613.2	18.6	120.7
8(2,6)–8(1,7)	80% (13/20)	52.0	327.1	13.2	58.3
10(2,8)–10(1,9)	45% (9/20)	33.5	98.3	9.7	19.0
		Thermal Detection Statistics			
3(2,1)–3(1,2)	40% (8/20)	28.5	48.4	8.9	21.9
5(2,3)–5(1,4)	50% (10/20)	34.5	55.4	10.6	21.5
8(2,6)–8(1,7)	40% (8/20)	38.0	48.8	12.4	17.6
10(2,8)–10(1,9)	30% (6/20)	41.0	39.5	14.4	17.4

Note. Columns 5 and 6 list the mean and median signal to noise (S$_{peak}$/N) for detections in each transition, where S$_{peak}$/N is calculated for each maser using the line rms from Table 2.

G28.83−0.25—We detect two weak 1.3 cm continuum sources (<0.4 mJy beam^{-1}; Table 4) coincident with this EGO. The eastern centimeter source, CM2, is also coincident with compact MIPSGAL 24 μm emission and 6.7 GHz CH$_3$OH masers (Cyganowski et al. 2009). The 1.3 cm emission from this source is spatially extended E–W, with a morphology consistent with multiple unresolved or marginally resolved sources (Figure 1). The western centimeter source, CM1, is unresolved and located $\sim$4″ west of CM2. Both CM1 and CM2 were detected by Cyganowski et al. (2011a) at 3.6 cm (but not at 1.3 cm; their 1.3 cm 4σ upper limit was 0.92 mJy beam^{-1}). Interestingly, at 3.6 cm, the western source (CM1 in both papers) is the brighter of the two, while at 1.3 cm, CM2 is the brighter source (Table 4 and Cyganowski et al. 2011a). This reversal suggests that CM2 either has a steeper free–free SED or more contribution from dust than CM1. We do not detect any 25 GHz CH$_3$OH emission above the 4σ level for this EGO. In at least three of the four CH$_3$OH lines there is, however, very weak emission ($\sim$3σ; so not included in our analysis), likely thermal, coincident with CM2.

G35.03+0.35—The 1.3 cm VLA survey data for this source were presented in Brogan et al. (2011). As shown in Figure 1, there is strong, spatially extended 1.3 cm continuum emission coincident with the EGO. Cyganowski et al. (2011a) resolved five distinct sources at 3.6 cm (denoted CM1,..., CM5). The two strongest (CM1 and CM2) were also detected by these authors at 1.3 cm, and CM2 is associated with 6.7 GHz CH$_3$OH masers (Cyganowski et al. 2009, 2011a; Surcis et al. 2015). The morphology of the 1.3 cm continuum emission in our VLA image is consistent with multiple, unresolved centimeter sources, and is spatially coincident with CM1, CM2, CM4, and CM5 from Cyganowski et al. (2011a). As we could not obtain satisfactory multicomponent fits to the current data, we report the combined total 1.3 cm flux density (18.5 mJy) as a single 1.3 cm source, which we denote CM1 (Table 4).

We detect one 25 GHz CH$_3$OH maser coincident with the 1.3 cm continuum emission, and one at the eastern edge of the extended 4.5 μm emission, coincident with an arc of 44 GHz Class I CH$_3$OH masers reported by Cyganowski et al. (2009). Brogan et al. (2011) reported the 25 GHz CH$_3$OH maser results from these VLA data, along with the detection of an NH$_3$ (3,3)

maser coincident with the 44 GHz Class I CH$_3$OH maser arc. Using H63α and H64α recombination lines, Brogan et al. (2011) find a velocity of 55.8 km s^{-1} for the free–free emission from CM1, in good agreement with the velocity of the coincident 25 GHz CH$_3$OH maser. Unfortunately, the Cyganowski et al. (2009) observations at 44 GHz only extend up to $\sim$54.4 km s^{-1}, and so the velocity at which the maser G35.03+0.35_a lies is not covered by the 44 GHz data. However, the spectrum presented in Kang et al. (2015) suggests an upper limit of $\sim$1 Jy.

G45.47+0.05—We detect strong, resolved 1.3 cm continuum emission coincident with the EGO and with the known UC H II region G45.47+0.05 (Wood & Churchwell 1989; Hofner et al. 1999), classified by Wood & Churchwell (1989) as "irregular or multiply peaked." In the new 1.3 cm VLA image, CM1 appears elongated along an NW–SE axis, suggestive of a possible ionized jet (Figure 1). The elongation direction of the cm-λ emission matches that of the extended 4.5 μm emission.

We detect both thermal and masing 25 GHz CH$_3$OH emission for this EGO, both coincident with a compact, southern component of CM1. The thermal emission is fairly compact compared to other thermal CH$_3$OH detections in the survey (1.61 × $<$0″.90), and has T_b = 24 K. The optically thin LTE calculations suggest a physical temperature of $T \sim 100$ K.

G49.27−0.34—We detect strong, resolved 1.3 cm continuum emission coincident with this EGO (Figure 1). This centimeter source, CM1, was detected by Cyganowski et al. (2011a) at 3.6 and 1.3 cm and by Mehringer (1994) at 20 cm; Cyganowski et al. (2011a) found that its cm-λ spectral index was consistent with optically thin free–free emission. The 1.3 cm continuum emission from CM1 exhibits a roughly circular morphology and is coincident with both extended 4.5 μm and 24 μm emission (see also the discussion in Cyganowski et al. 2011a). We do not detect a 1.3 cm counterpart to the weak, compact Cyganowski et al. (2011a) 3.6 cm source CM2 (0.61 mJy beam^{-1} at 3.6 cm) at the $>$4σ level (4σ limit of 0.28 mJy beam^{-1} compared to 0.71 mJy beam^{-1} in Cyganowski et al. 2011a). Neither thermal nor masing 25 GHz CH$_3$OH emission is detected toward this EGO.

4. Discussion

4.1. Spatial Distribution of 25 GHz CH₃OH Emission Compared to 4.5 μm Emission

The overall correlation between 25 GHz CH$_3$OH emission and extended 4.5 μm emission is strong. In only two of our target regions is the 25 GHz emission entirely outside the boundaries of the extended 4.5 μm emission. In these cases (G10.29−0.13 and G28.28−0.36), the relationship between the 4.5 μm emission and the 25 GHz CH$_3$OH masers is unclear. In total, 25 of our 34 detected maser sites (74%) are coincident with extended 4.5 μm emission. The nine masers that are not coincident with extended 4.5 μm emission are predominantly located near dark clouds (Figure 1).

Nine of the ten thermal CH$_3$OH detections (90%) are coincident with extended 4.5 μm emission (see Table 6); of these, all but one (G14.63−0.58) is also coincident with strong 24 μm emission (Figure 1). The exception is the thermal CH$_3$OH emission in G08.67−0.35, which is not coincident with the extended 4.5 μm emission but is instead coincident with 1.3 cm continuum emission and the known H II region G8.67−0.36 (Wood & Churchwell 1989; see also Section 3.3).

4.2. Spatial Distribution of 25 GHz CH₃OH Emission Compared to 1.3 cm Continuum Emission

We find a strong correlation between the presence of thermal CH$_3$OH emission at 25 GHz and the presence of 1.3 cm continuum emission. Nine of our ten thermal emission detections (90%) are coincident with a 1.3 cm detection (see Table 6). The exception is G10.34−0.14, which shows one thermal emission site but has no detected 1.3 cm continuum emission coincident with the EGO. However, there is strong 1.3 cm continuum emission to the south from the W31 star-forming complex, and this causes the G10.34−0.14 field to have one of the poorer continuum sensitivities due to dynamic range limitations. This may be limiting our ability to detect weak 1.3 cm emission toward the EGO in this case.

While sources that have thermal CH$_3$OH almost always have 1.3 cm continuum emission, we find that the reverse is not true: of our 19 sources of 1.3 cm emission, only nine (47%) have coincident thermal CH$_3$OH emission. In addition, we also find only a weak correlation between the presence of 25 GHz CH$_3$OH maser emission and the presence 1.3 cm continuum emission, with only only eight masers (24%) coincident with the continuum (where we define "coincident" as being within the boundary of the 4σ level of the 1.3 cm emission), while the other 26 masers lie outside the boundaries of any 1.3 cm continuum.

4.3. Correlation between 6.7 GHz CH₃OH Masers, 1.3 cm Continuum, and Thermal 25 GHz CH₃OH Emission

Interestingly, 6.7 GHz Class II CH$_3$OH masers do appear to be correlated with both 1.3 cm continuum and 25 GHz thermal CH$_3$OH emission in our EGO sample. Nineteen of the 1.3 cm sources are in regions for which past 6.7 GHz data exist in the literature (the exception being G14.33−0.64_a, Table 1). Twelve of these nineteen 1.3 cm sources (63%) are coincident with 6.7 GHz masers (Section 3.3); of these, eight are new detections at 1.3 cm, and four (G14.63_CM1, G18.67_CM1, G19.36_CM2, and G22.04_CM1) are, to our knowledge, new detections at any cm-λ. Conversely, 12 of the 18 Class II

6.7 GHz CH$_3$OH masers associated with our target EGOs (67%) are coincident with 1.3 cm emission in the VLA images. Of the six 6.7 GHz masers without cm-λ detections, three are in regions (G10.29−0.13, G10.34−0.14, and G28.28−0.36) that have two to six times poorer sensitivity than the majority of the sample due to dynamic range limitations (Table 2). The detection of weak cm-λ continuum emission associated with Class II CH$_3$OH masers is consistent with both phenomena tracing young, deeply embedded massive (proto)stars. Similarly, thermal 25 GHz CH$_3$OH emission in the VLA data may pinpoint hot core emission, which has been observed in association with 6.7 GHz masers in large-scale single-dish surveys (e.g., Purcell et al. 2006, 2009). Of the 10 sources of thermal 25 GHz CH$_3$OH emission seen with the VLA, eight are coincident with 6.7 GHz masers. The exceptions are G14.63−0.58_a, in which the thermal CH$_3$OH emission is coincident with the weaker centimeter source CM2 but the 6.7 GHz masers are coincident with the stronger centimeter source CM1, and G45.47+0.05_a, which has thermal CH$_3$OH emission but no 6.7 GHz masers. High-resolution observations in other hot core tracers (e.g., with (sub)millimeter interferometers) will illuminate the nature of these objects.

4.4. Detailed Comparison of 25 GHz and 44 GHz Class I CH₃OH Masers

Current models for the pumping of Class I CH$_3$OH masers suggest that 25 GHz masers are excited under an overlapping but narrower region of parameter space than 44 GHz masers (Sobolev et al. 2007). Thus, we do not expect 25 GHz masers to be present without a 44 GHz counterpart. In order to test this hypothesis observationally, we compare our 25 GHz CH$_3$OH maser properties with the 44 GHz CH$_3$OH maser results from the VLA survey of Cyganowski et al. (2009). Of the 13 EGO fields with 25 GHz CH$_3$OH maser detections, seven were also included in the Cyganowski et al. (2009) survey. A total of 17 individual 25 GHz CH$_3$OH masers were detected toward the EGOs in common between the two surveys. Of these 17 masers, two (G10.29−0.13_b and G35.03+0.35_a) do not have complementary 44 GHz data because the spectral breadth of the 44 GHz observations did not cover the 25 GHz maser velocity. This leaves 15 masers with interferometric observations at both 25 and 44 GHz. In order to compare the 25 and 44 GHz CH$_3$OH masers, we first regridded the Cyganowski et al. (2009) 44 GHz image cubes (with a channel width of 0.17 km s^{-1}) to 0.4 km s^{-1} channels to match the 25 GHz data. After testing, we elected not to convolve the 44 GHz image cubes to the poorer angular resolution of the 25 GHz data. The 44 GHz data have significantly higher angular resolution ($0\farcs5$–$1\farcs0$) for most sources, and there are typically many more 44 GHz masers in a given region than 25 GHz masers (see Figure 1). Preserving the higher angular resolution of the 44 GHz data allows us to pinpoint which 44 GHz maser provided the closest positional match for each 25 GHz detection.

For each of the fifteen 25 GHz masers with 44 GHz data, the properties of the 44 GHz maser in closest positional and kinematic proximity (typically matching to within one channel) were fit using the procedure described in Section 3.2. We then compared the 25 GHz (5_2 transition) and 44 GHz fitted
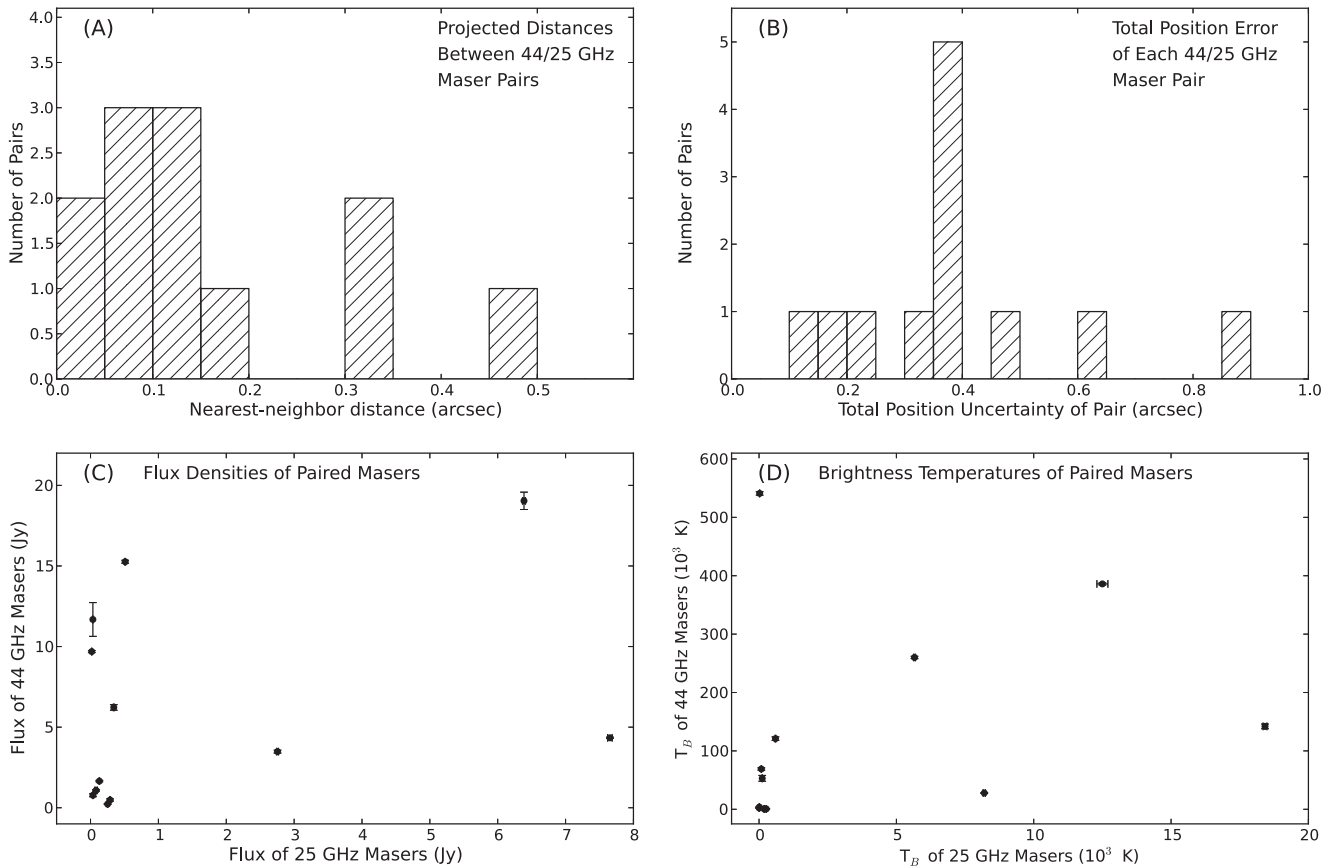
Figure 4. (a) Nearest-neighbor distances, (b) position uncertainties, (c) 44 GHz vs. 25 GHz fluxes, and (d) 44 GHz vs. 25 GHz brightness temperatures of paired masers.

positions (Figure 4(a)), and considered them a pair if

$$\Delta\theta_{\text{sep}} < \sqrt{\sigma^2_{\text{R.A.-25}} + \sigma^2_{\text{Decl.-25}}} + \sqrt{\sigma^2_{\text{R.A.-44}} + \sigma^2_{\text{Decl.-44}}} + 0.1\theta_{25_{\text{beam}}}, \tag{1}$$

where $\Delta\theta_{\text{sep}}$ is the angular separation, in arcseconds, between the fitted positions of the 25 and 44 GHz masers. The quantity on the right is the angular separation threshold (σ_{pos}), which consists of the sum of three terms: $\sigma_{\text{R.A.}}$ and $\sigma_{\text{Decl.}}$ are the errors on the fitted positions of the 25 and 44 GHz masers in arcseconds, and the final term is one-tenth the geometric mean of the synthesized beam of the 25 GHz data (in arcseconds). We add this additional factor to account for the extra uncertainty introduced because the two data sets were observed at different times and with different phase calibrators, so the absolute positions might differ by up to $0.1\theta_{\text{beam}}$ even when the fitted position uncertainties of the individual masers are quite small.

Of the 25 GHz CH_3OH masers with complementary 44 GHz data, 12 of 15 have 44 GHz counterparts with $\Delta\theta_{\text{sep}} < 1\sigma_{\text{pos}}$; we consider these to be "pairs," i.e., spatially coincident. Figures 4(a) and (b) show the distributions of maser separations and $1\sigma_{\text{pos}}$ values for the paired masers; as shown in Figure 4(a), maser pairs are co-located within $0\!\!.''5$. The three remaining 25 GHz masers have 44 GHz counterparts within $\Delta\theta_{\text{sep}}$ of 1.15 to $1.43\sigma_{\text{pos}}$. These masers—G19.36−0.03_b, G19.36−0.03_c, and G28.28−0.36_a—have fitted 25 GHz 5_2 flux densities of 91 ± 4 mJy, 46 ± 2 mJy, and 93 ± 7 mJy, respectively. While on the lower end of our observed range, these flux densities are

by no means exceptional. It is notable that in general, there does not appear to be a correlation between the flux density of the 5_2 transition and the nearest-neighbor distance. It is possible that for these two regions (G19.36−0.03 and G28.28−0.36) there is a greater absolute position mismatch than for the other targets. Thus, at the present angular resolution, it is plausible that all 25 GHz masers have a detectable 44 GHz counterpart. Higher resolution observations in multiple maser transitions would be useful to further constrain the exact position coincidence and also the physical size of the maser spots.

The 25 GHz CH_3OH masers are weaker than their 44 GHz counterparts by a median factor of 13. The two exceptions are G22.04+0.22_a and G35.03+0.35_b, which are stronger than their counterparts by factors of 1.8 and 1.1, respectively. Notably, we find no correlation between the 25 GHz and 44 GHz maser flux densities or brightness temperatures for paired masers (Figures 4(c)–(d)), which is consistent with the results of Voronkov et al. (2007), who found no correlation between the flux densities of 25 GHz and other Class I CH_3OH masers. Both 44 and 25 GHz CH_3OH masers have also been observed to exhibit variations in brightness on a range of timescales (Pratap et al. 2007; Sobolev et al. 2007), so the difference in observation dates between the 44 and 25 GHz data may contribute to the lack of correlation in the flux densities. Furthermore, 44 GHz masers arise from A-type CH_3OH, while 25 GHz masers arise from E-type CH_3OH; thus, it is possible that this difference in parity also contributes to the lack of correlation between maser flux densities. Finally, despite the high detection rate (85%) of 95 GHz Class I maser emission from our sample (Table 1), we cannot perform a similar

comparison with the 25 GHz maser results due to the absence of interferometric observations in the higher frequency line.

4.5. Comparison with Millimeter Molecular Line Surveys of EGOs

Here we focus on comparison with other molecular line surveys of EGOs that target complex molecules ($\geqslant 6$ atoms; Herbst & van Dishoeck 2009) and include a significant fraction of our sample. He et al. (2012) conducted a survey of 89 northern EGOs ($\delta > -38°$) with the Arizona Radio Observatory Submillimeter Telescope (ARO SMT; beam size $\sim 29''$) in multiple transitions of $H^{13}CO^+$, SiO, SO, CH_3OH, CH_3OCH_3, CH_3CH_2CN, $HCOOCH_3$, and $HN^{13}C$, c-HCCCH, and H_2CCO, as well as the unidentified line U260365. They detected 18 of the EGOs in our VLA sample in one or more transitions (G08.67−0.35 was not targeted and G25.27−0.43 was targeted but not detected). We compared their detection rates in each line to our EGOs with and without 25 GHz thermal CH_3OH emission to search for a correlation between the presence of 25 GHz thermal CH_3OH and other species. We find that sources with thermal 25 GHz CH_3OH have higher overall detection rates (considering all observed transitions) in He et al. (2012) than sources without thermal CH_3OH. However, this difference is primarily due to the higher detection rates that our sample have in the He et al. (2012) sample, specifically in the CH_3OH lines. Sources with 25 GHz thermal CH_3OH have a typical detection rate of 67%–78% in the CH_3OH lines of the He sample, while the sources without thermal CH_3OH have a typical detection rate of only 30%–40%. Detection rates among non-CH_3OH species are about the same for sources with and without 25 GHz thermal CH_3OH. The only such species detected in the majority of our sources are $H^{13}CO^+$, SiO, and SO, and these detection rates are equally high for sources with and without 25 GHz thermal CH_3OH. Although we do not find a correlation between thermal CH_3OH in our sample and any particular non-CH_3OH species, we do find that sources with thermal CH_3OH are detected in a greater *number* of non-CH_3OH species than those without, indicating a possible correlation between the presence of 25 GHz thermal CH_3OH emission and a richer gas chemistry.

Ge et al. (2014) use the data of He et al. (2012) to determine rotational temperatures and abundances for four of the species observed (CH_3OH, CH_3OCH_3, $HCOOCH_3$, and CH_3CH_2CN). They list results for seven of the EGOs with 25 GHz thermal CH_3OH and for four of the EGOs without. The EGOs with thermal CH_3OH do not appear to be significantly hotter or cooler than those without, based on these rotational temperatures. The median CH_3OH abundance of the EGOs with thermal CH_3OH is 1.43×10^{-9} and 1.06×10^{-9} for those without. While the abundance is slightly higher for sources with 25 GHz thermal CH_3OH, it is worth noting that the source with the highest abundance, G14.33−0.64, has an abundance a factor of ten higher than the median but does not have detectable 25 GHz thermal CH_3OH emission at the current sensitivity.

5. Conclusions

In a high-resolution VLA survey of 20 EGOs in the Milky Way, we identify 34 sites of 25 GHz Class I CH_3OH maser emission, 10 sites of thermal CH_3OH emission, and 20 sources of 1.3 cm continuum emission. Thirteen of the continuum sources are new detections at 1.3 cm, having a typical peak intensity of 0.5 mJy beam^{-1}. To our knowledge, seven of these objects are new detections at any cm-λ, while 12 are either coincident with or within $2''$ of 6.7 GHz Class II CH_3OH maser emission. Regardless of the type of CH_3OH emission (maser or thermal), it is strongly correlated in position with 4.5 μm EGO emission. We also find a strong correlation between the presence of thermal CH_3OH emission and the presence of 1.3 cm continuum emission, with the two occurring coincidentally in 9 out of 10 cases (see Section 3.3 for a discussion of the lone exception to this trend, G10.34−0.14). Note that the inverse relation is not true: of the 20 sources of 1.3 cm emission, only nine have coincident thermal CH_3OH emission. While there is a correlation between the *presence* of 1.3 cm emission and 25 GHz Class I CH_3OH masers, there is an anti-correlation between their *positions*. Specifically, of our 16 targets with both 1.3 cm continuum and CH_3OH line emission, 10 have 25 GHz CH_3OH maser emission. However, only 8 of 34 masers lie within the boundaries of the 4σ contours of the 1.3 cm continuum emission.

For the sites classified as maser emission, the fitted flux densities are strongest in the 5_2 transition (see Table 7), but the 8_2 transition is not significantly weaker than the 5_2 transition in general. The rarest transition is 10_2, which is detected in only 45% of targets compared to the 60% detection rate for 3_2 and the 80% detection rates for 5_2 and 8_2. For the 25 GHz masers for which we have complementary 44 GHz Class I CH_3OH maser data, we find likely or possible 44 GHz companions for every 25 GHz maser, which is consistent with the suggestion that Class I CH_3OH masers at 25 and 44 GHz trace similar excitation conditions (Sobolev et al. 2007). In general, the 25 GHz masers are significantly weaker than their 44 GHz counterparts; however, we do not find any correlation between the flux densities or brightness temperatures of the paired masers. Higher matched resolution observations of masers at both wavelengths are needed in order to further constrain both the brightness temperatures and exact positions of each 25 GHz and 44 GHz maser.

References

Barrett, A. H., Ho, P., & Martin, R. N. 1975, ApJL, 198, L119
Barrett, A. H., Schwartz, P. R., & Waters, J. W. 1971, ApJL, 168, L101
Benjamin, R. A., Churchwell, E., Babler, B. L., et al. 2003, PASP, 115, 953
Beuther, H., Zhang, Q., Sridharan, T. K., Lee, C.-F., & Zapata, L. A. 2006, A&A, 454, 221
Breen, S. L., & Ellingsen, S. P. 2011, MNRAS, 416, 178
Brogan, C. L., Hunter, T. R., Cyganowski, C. J., et al. 2011, ApJL, 739, L16
Brogan, C. L., Hunter, T. R., Cyganowski, C. J., et al. 2016, ApJ, 832, 187
Carey, S. J., Noriega-Crespo, A., Mizuno, D. R., et al. 2009, PASP, 121, 76
Caswell, J. L. 2009, PASA, 26, 454
Chandler, C. J., & Butler, B. J. 2014, Proc. SPIE, 9149, 914917
Chen, X., Ellingsen, S. P., He, J.-H., et al. 2012, ApJS, 200, 5

Chen, X., Ellingsen, S. P., Shen, Z.-Q., Titmarsh, A., & Gan, C.-G. 2011, ApJS, 196, 9

Chen, X., Gan, C.-G., Ellingsen, S. P., et al. 2013, ApJS, 206, 9

Churchwell, E., Babler, B. L., Meade, M. R., et al. 2009, PASP, 121, 213

Cragg, D. M., Johns, K. P., Godfrey, P. D., & Brown, R. D. 1992, MNRAS, 259, 203

Cyganowski, C. J., Brogan, C. L., Hunter, T. R., et al. 2012, ApJL, 760, L20

Cyganowski, C. J., Brogan, C. L., Hunter, T. R., et al. 2014, ApJL, 796, L2

Cyganowski, C. J., Brogan, C. L., Hunter, T. R., et al. 2017, arXiv:1701.02802

Cyganowski, C. J., Brogan, C. L., Hunter, T. R., & Churchwell, E. 2009, ApJ, 702, 1615

Cyganowski, C. J., Brogan, C. L., Hunter, T. R., & Churchwell, E. 2011a, ApJ, 743, 56

Cyganowski, C. J., Brogan, C. L., Hunter, T. R., Churchwell, E., & Zhang, Q. 2011b, ApJ, 729, 124

Cyganowski, C. J., Koda, J., Rosolowsky, E., et al. 2013, ApJ, 764, 61

Cyganowski, C. J., Whitney, B. A., Holden, E., et al. 2008, AJ, 136, 2391

Ellingsen, S. P. 2006, ApJ, 638, 241

Ge, J. X., He, J. H., Chen, X., & Takahashi, S. 2014, MNRAS, 445, 1170

Gómez, L., Luis, L., Hernández-Curiel, I., et al. 2010, ApJS, 191, 207

Green, J. A., Caswell, J. L., Fuller, G. A., et al. 2010, MNRAS, 409, 913

He, J. H., Takahashi, S., & Chen, X. 2012, ApJS, 202, 1

Herbst, E., & van Dishoeck, E. F. 2009, ARA&A, 47, 427

Hills, R., Pankonin, V., & Landecker, T. L. 1975, A&A, 39, 149

Hofner, P., & Churchwell, E. 1996, A&AS, 120, 283

Hofner, P., Kurtz, S., Ellingsen, S. P., et al. 2011, ApJL, 739, L17

Hofner, P., Peterson, S., & Cesaroni, R. 1999, ApJ, 514, 899

Ilee, J. D., Cyganowski, C. J., Nazari, P., et al. 2016, MNRAS, 462, 4386

Immer, K., Galván-Madrid, R., König, C., Liu, H. B., & Menten, K. M. 2014, A&A, 572, A63

Jaffe, D. T., Stier, M. T., & Fazio, G. G. 1982, ApJ, 252, 601

Johnston, K. J., Gaume, R., Stolovy, S., et al. 1992, ApJ, 385, 232

Kang, H., Kim, K.-T., Byun, D.-Y., Lee, S., & Park, Y.-S. 2015, ApJS, 221, 6

Kurtz, S., Churchwell, E., & Wood, D. O. S. 1994, ApJS, 91, 659

Kurtz, S., Hofner, P., & Álvarez, C. V. 2004, ApJS, 155, 149

Leurini, S., Menten, K. M., & Walmsley, C. M. 2016, A&A, 592, A31

Li, F. C., Xu, Y., Wu, Y. W., et al. 2016, AJ, 152, 92

Lu, X., Zhang, Q., Liu, H. B., Wang, J., & Gu, Q. 2014, ApJ, 790, 84

Matsakis, D. N., Wright, M. C. H., Townes, C. H., et al. 1980, ApJ, 236, 481

Mehringer, D. M. 1994, ApJS, 91, 713

Menten, K. M., Walmsley, C. M., Henkel, C., & Wilson, T. L. 1986, A&A, 157, 318

Menten, K. M., Walmsley, C. M., Henkel, C., & Wilson, T. L. 1988, A&A, 198, 267

Moscadelli, L., Cesaroni, R., Sánchez-Monge, Á., et al. 2013, A&A, 558, A145

Moscadelli, L., Sánchez-Monge, Á., Goddi, C., et al. 2016, A&A, 585, A71

Müller, H. S. P., Menten, K. M., & Mäder, H. 2004, A&A, 428, 1019

Perley, R. A., Chandler, C. J., Butler, B. J., & Wrobel, J. M. 2011, ApJL, 739, L1

Plambeck, R. L., & Menten, K. M. 1990, ApJ, 364, 555

Pratap, P., Strelnitski, V., Hoffman, S., & Lemonias, J. 2007, in IAU Symp. 242, Astrophysical Masers and their Environments, ed. J. M. Chapman & W. A. Baan (New York, NY: Cambridge Univ. Press)

Purcell, C. R., Balasubramanyam, R., Burton, M. G., et al. 2006, MNRAS, 367, 553

Purcell, C. R., Longmore, S. N., Burton, M. G., et al. 2009, MNRAS, 394, 323

Rathborne, J. M., Jackson, J. M., & Simon, R. 2006, ApJ, 641, 389

Rathborne, J. M., Simon, R., & Jackson, J. M. 2007, ApJ, 662, 1082

Reid, M. J., Menten, K. M., Brunthaler, A., et al. 2014, ApJ, 783, 130

Rosero, V., Hofner, P., Claussen, M., et al. 2016, ApJS, 227, 25

Sanna, A., Moscadelli, L., Cesaroni, R., et al. 2010, A&A, 517, A71

Sobolev, A. M., Cragg, D. M., Ellingsen, S. P., et al. 2007, in IAU Symp. 242, Astrophysical Masers and their Environments, ed. J. M. Chapman & W. A. Baan (New York, NY: Cambridge Univ. Press), 81

Stahler, S. W., Palla, F., & Ho, P. T. P. 2000, in Protostars and Planets IV, ed. V. Mannings, A. P. Boss, & S. S. Russell (Tucson, AZ: Univ. of Arizona Press), 327

Surcis, G., Vlemmings, W. H. T., van Langevelde, H. J., et al. 2015, A&A, 578, A102

Szymczak, M., Pillai, T., & Menten, K. M. 2005, A&A, 434, 613

Val'tts, I. E., Ellingsen, S. P., Slysh, V. I., et al. 2000, MNRAS, 317, 315

Voronkov, M. A., Brooks, K. J., Sobolev, A. M., et al. 2006, MNRAS, 373, 411

Voronkov, M. A., Caswell, J. L., Ellingsen, S. P., et al. 2012, in IAU Symp. 287, Cosmic Masers—from OH to H0, ed. R. S. Booth, E. M. L. Humphreys, & W. H. T. Vlemmings (New York, NY: Cambridge Univ. Press), 433

Voronkov, M. A., Sobolev, A. M., Ellingsen, S. P., et al. 2007, in IAU Symp. 242, Astrophysical Masers and their Environments, ed. J. M. Chapman & W. A. Baan (New York, NY: Cambridge Univ. Press)

Wenger, M., Ochsenbein, F., Egret, D., et al. 2000, A&AS, 143, 9

Westerhout, G. 1958, BAN, 14, 215

Wood, D. O. S., & Churchwell, E. 1989, ApJS, 69, 831

Yorke, H. W., Bodenheimer, P., & Laughlin, G. 1993, ApJ, 411, 274

Zapata, L. A., Rodríguez, L. F., Ho, P. T. P., Beuther, H., & Zhang, Q. 2006, AJ, 131, 939

Zinnecker, H., & Yorke, H. W. 2007, ARA&A, 45, 481